An olivine cumulate outcrop on the floor of Jezero crater, Mars

Y Liu, M M Tice, M E Schmidt, A H Treiman, T V Kizovski, J A Hurowitz, A C Allwood, J Henneke, D a K Pedersen, S J Vanbommel, et al.

Title: An olivine cumulate outcrop on the floor of Jezero crater, Mars

Authors: Y. Liu[1,*], M.M. Tice[2], M.E. Schmidt[3], A.H. Treiman[4], T.V. Kizovski[3], J.A. Hurowitz[5], A.C. Allwood[1], J. Henneke[6], D.A.K. Pedersen[6], S.J. VanBommel[7], M.W.M. Jones[8], A.L. Knight[7], B.J. Orenstein[9], B.C. Clark[10], W.T. Elam[11], C.M. Heirwegh[1], T. Barber[1], L.W. Beegle[1], K. Benzerara[12], S. Bernard[12], O. Beyssac[12], T. Bosak[13], A.J. Brown[14], E.L. Cardarelli[1], D.C. Catling[15], J.R. Christian[7], E.A. Cloutis[16], B.A. Cohen[17], S. Davidoff[1], A.G. Fairén[18,19], K.A. Farley[20], D.T. Flannery[9], A. Galvin[1], J.P. Grotzinger[20], S. Gupta[21], J. Hall[13], C.D.K. Herd[22], K. Hickman-Lewis[23, 24], R.P. Hodyss[1], B.H.N. Horgan[25], J.R. Johnson[26], J.L. Jørgensen[6], L.C. Kah[27], J.N. Maki[1], L. Mandon[28], N. Mangold[29], F.M. McCubbin[30], S.M. McLennan[5], K. Moore[20], M. Nachon[2], P. Nemere[9], L.D. Nothdurft[9], J.I. Núñez[26], L. O'Neil[11], C.M. Quantin-Nataf[31], V. Sautter[12], D.L Shuster[32], K.L. Siebach[33], J.I. Simon[30], K.P. Sinclair[11], K.M. Stack[1], A. Steele[34], J.D. Tarnas[1], N.J. Tosca[35], K. Uckert[1], A. Udry[36], L.A. Wade[1], B.P. Weiss[13], R.C. Wiens[37], K.H. Williford[1,38], M.-P. Zorzano[18]

Affiliations:

[1]Jet Propulsion Laboratory, California Institute of Technology, Pasadena, CA 91109, USA
[2]Department of Geology & Geophysics, Texas A&M University, College Station, TX 77843, USA
[3]Department of Earth Sciences, Brock University, St. Catharines, ON L2S 3A1, Canada
4 Lunar and Planetary Institute, Universities Space Research Association, Houston TX 77058, USA
[5]Department of Geosciences, Stony Brook University, Stony Brook, NY 11794, USA
[6]Department of Space, Measurement and Instrumentation, Technical University of Denmark, , Lyngby, Denmark
[7]McDonnell Center for the Space Sciences, Department of Earth and Planetary Sciences, Washington University in St. Louis, St. Louis, MO 63130, USA
[8]Central Analytical Research Facility, and School of Chemistry and Physics, Queensland University of Technology, Brisbane, QLD 4000, Australia
[9]School of Earth & Atmospheric Sciences, Queensland University of Technology, Brisbane, QLD 4000, Australia
[10]Space Science Institute, Boulder, CO 80301, USA
[11]Applied Physics Lab and Department of Earth and Space Sciences, University of Washington, Seattle, WA 98052, USA
[12] Institut de Minéralogie, Physique des Matériaux et Cosmochimie, Centre National de la Recherche Scientifique, Muséum National d'Histoire Naturelle,Sorbonne Université, Paris 75005, France
[13]Department of Earth, Atmospheric and Planetary Sciences, Massachusetts Institute of Technology, Cambridge, MA 02139, USA
[14]Plancius Research, MD 21146, USA
[15]Department of Earth and Space Sciences, University of Washington, Seattle WA 98195, USA
[16]Department of Geography, University of Winnipeg, Winnipeg, Manitoba R3B 2E9, Canada
[17]NASA Goddard Space Flight Center, Greenbelt, MD 20771, USA
[18]Centro de Astrobiología, Consejo Superior de Investigaciones Cientificas - Instituto Nacional de Tecnica Aeroespacial), Madrid 28850, Spain
[19] Dept. of Astronomy, Cornell University, Ithaca, NY 14853, USA
[20]Division of Geological and Planetary Sciences, California Institute of Technology, Pasadena, CA 91125, USA
[21]Department of Earth Science and Engineering, Imperial College London, London SW7 2AZ, UK
[22]Department of Earth and Atmospheric Sciences, University of Alberta, Edmonton, Alberta T6G 2E3, Canada
[23]Department of Earth Sciences, The Natural History Museum, South Kensington, London, SW7 5BD, UK

[24]Dipartimento di Scienze Biologiche, Geologiche e Ambientali, Università di Bologna, via Zamboni 67, I-40126 Bologna, Italy
[25]Department of Earth, Atmospheric, and Planetary Sciences, Purdue University, West Lafayette, IN 47907, USA
[26]Johns Hopkins University Applied Physics Laboratory Laurel, MD 20723, USA
[27]Department of Earth and Planetary Sciences, University of Tennessee, Knoxville TN 37996, USA
[28] Laboratoire d'Etudes Spatiales et d'Instrumentation en Astrophysique, Observatoire de Paris-PSL, CNRS, Sorbonne Université, Université de Paris Cité, Meudon 92190, France
[29]Laboratoire Planetologie et Geosciences, Centre National de Recherches Scientifiques, Universite Nantes, Universite Angers, Unite Mixte de Recherche 6112, Nantes 44322, France
[30]NASA Johnson Space Center, Houston, TX 77058, USA
[31]Laboratoire de Geologie de Lyon-Terre Planetes Environnement, Univ Lyon, Universite Claude Bernard Lyon 1, Ecole Normale Superieure Lyon, Centre National de Recherches Scientifiques, 69622 Villeurbanne, France
[32]Dept. Earth and Planetary Science, University of California, Berkeley, CA 94720, USA
[33]Department of Earth, Environmental, and Planetary Sciences, Rice University, Houston, TX 77005, USA
[34]Earth and Planets Laboratory, Carnegie Institution for Science, Washington, DC 20015, USA
[35]Department of Earth Sciences, University of Cambridge, Cambridge, CB2 3EQ, UK
[36]Department of Geosciences University of Nevada Las Vegas, Las Vegas, NV 89154, USA
[37]Los Alamos National Laboratory, Los Alamos, NM 87545, USA
[38]Blue Marble Space Institute of Science, 600 1st Ave. Seattle, WA 98104, USA

*Corresponding author, Email: yang.liu@jpl.nasa.gov.

Abstract: The geological units on the floor of Jezero crater, Mars, are part of a wider regional stratigraphy of olivine-rich rocks, which extends well beyond the crater. We investigate the petrology of olivine and carbonate-bearing rocks of the Séítah formation in the floor of Jezero. Using multispectral images and x-ray fluorescence data, acquired by the Perseverance rover, we performed a petrographic analysis of the Bastide and Brac outcrops within this unit. We find that these outcrops are composed of igneous rock, moderately altered by aqueous fluid. The igneous rocks are mainly made of coarse-grained olivine, similar to some Martian meteorites. We interpret them as an olivine cumulate, formed by settling and enrichment of olivine through multi-stage cooling of a thick magma body.

Main Text:

Jezero crater, the landing site of the Perseverance rover, is constrained in age between 3.82 and 3.96 billion-yeas and is located at the western edge of Isidis Planitia on Mars (*1*, *2*) (**Fig. 1A**). The Séítah formation, informally named, is a light-toned, olivine- and carbonate-bearing rock unit exposed on the floor of Jezero (*3*-5) (**Fig. 1C**). Morphologically and mineralogically similar rocks extend beyond the rim of Jezero, spanning >70,000 km^2 from inside Isidis Planitia (*6*), to the neighboring regions of Northeast Syrtis (*7*), Nili Fossae (*8*), and Libya Montes (*9*, *10*) (**Fig. 1B**). Orbital observations have shown this regional unit has high abundances of olivine (*11*), an early crystallizing, rock-formimg mineral, with large inferred grain sizes (several millimeters) and moderate magnesium contents ($Fo_{44-66,}$ Fo is Fo#, the mole percent of forsterite, Mg_2SiO_4, in olivine) (*4,11*). Hypotheses for the unit's origin include an impact melt or intrusive igneous rocks

(*6*), basaltic lava flows (*9*, *12*), volcanic ash (*2*, *13*) or clastic material (i.e., fragmental deposits formed by transport and deposition from volcanic eruptions, impacts, water, or wind) (*14*).

Images of Séítah formation rocks taken by the Perseverance rover have shown centimeter- to decimeter-scale layering and abundant dark, millimeter-scale angular grains, reported in a companion paper (*5*). These observations were consistent with any of the above hypotheses for the regional unit's origin. We sought to distinguish between these possibilities using the rover's arm-mounted Planetary Instrument for X-ray Lithochemistry (PIXL) (*15*).

PIXL observations

To remove any modified surface materials, two 50 mm diameter patches (informally named Garde and Dourbes) were abraded into two rock outcrops (informally named Bastide and Brac, respectively). Both outcrops are part of the Bastide member (informally named) of the Séítah formation (**Fig. 1C**). Reflectance optical images of both patches illuminated by ultraviolet (UV, 385 nm), blue (B, 450 nm), green (G, 530 nm) and near-infrared (735 nm) light emitting diodes (LEDs) were acquired using PIXL's micro context camera (MCC). The Dourbes patch was subsequently analyzed by two x-ray fluorescence (XRF) raster maps with areas of 4 × 12.5 mm and 5 × 7 mm at a step size of 0.125 mm, respectively (**Fig. 1)** (*16*).

We use these data to produce color and color ratio images of both patches, and estimate volume percentages of phases in each (**Figs. 2A and S1, Table S1**). For the Dorubes patch where XRF maps were acquired, we produce diffraction maps of crystallinity and crystal orientation (**Figs. 2C and S2**), composite maps of elemental abundances (**Figs. 2D, S3, and S4**), and chemical analyses of individual minerals and the bulk rock (**Tables S2-S3**) (see the Methods in *16*). The reconstructed color images show both patches display a similar texture, with beige equant grains of sizes range from 1 to 3.5 mm, greenish gray irregularly shaped grains, and reddish brown materials rimming these grains or occupying irregular areas between them (**Fig. S1A**). These features are discernable in color ratio plots (**Figs. 2A and S1**). Elemental maps show inter-grain areas contain distinct chemical variations, and reveal additional irregular regions with high Al (**Figs. 2D**) and non-uniform distribution of Na, K, and P (**Fig. S3**).

Our identifications of olivine and pyroxene minerals are supported by stoichiometric analysis of the PIXL data and are consistent with observations by other Perseverance instruments (*5*). We find the beige equant grains have molar (Mg+Fe)/Si ≈ 2 and total cations of 2.995 - 3.025 for 4 oxygens (**Table S2**), consistent with olivine's chemical formula as $(FeMg)_2SiO_4$. The greenish gray grains have molar (Ca+Mg+Fe)/Si ≈ 1 and total cations of 4.032 – 4.042 for 4 oxygens (**Table S2**), consistent with pyroxene's formula as $(CaFeMg)_2Si_2O_6$. The molar Ca/(Ca+Mg+Fe) ratios of pyroxene (0.35 to 0.37) show that it is augite **(Fig. 3A)** as defined by *(17)*. Back-reflected diffracted x-rays from some non-contiguous augite regions show that they have identical crystal orientations, indicating these regions are likely to be part of the same three-dimensional grain (i.e., a single augite crystal) (**Figs. 2C and S2**). This texture, where a large single pyroxene grain encloses smaller olivine grains (poikilitic texture), is characteristic of igneous cumulate rocks (**Fig. 2A-2B**). The irregular inter-grain Al-rich areas contain intergrown grains of Na-rich feldspar (<1 mm), Fe-Cr-Ti oxide (≤0.25 mm), K-rich feldspar (<0.125 mm) and Ca-phosphate (<0.125 mm), which are typical features of mesostasis – the last formed materials in the intergranular space – in igneous rocks (**Figs. S3 and S4**). Olivine, augite, and mesostasis are the primary minerals in the pre-alteration bedrocks in the Séítah formation. The inter-grain reddish brown materials contain silicates, Fe-Mg carbonate, and Fe-Mg sulfate, which are secondary materials from alteration. The presence of carbonates was also indicated by other

instruments on Perseverance (*5*) and consistent with oribital observations. In this report, we focus on primary minerals.

Olivine is the dominant primary mineral, making up 65 ± 5 vol% of the Dourbes and Garde rocks (**Fig. S1B, Table S1**). The remainder of the analyzed area is made of augite at ~13 vol%, mesostasis at ~10 vol%, and secondary materials at ~12 vol %. The relative mineral proportions of olivine, augite, and feldspar indicate Dourbes is an olivine-rich wehrlite, which is an ultramafic igneous rock based on the classification in (*18*) (**Fig. 3C**).

The chemical compositions of olivine grains ($Fo_{55\pm1}$) are uniform, both within and between grains (**Fig. 3B, Table S2**). Olivine grains contain more Fe than that would be in equilibrium with a melt of the rocks' bulk composition (**Tables S2 and S5, Fig. S5**). The augite chemistry ($Wo_{35-38}En_{43-44}Fs_{20-21}$) is expressed as mole% of wollastonite (Wo, $Ca_2Si_2O_6$), enstatite (En, $Mg_2Si_2O_6$), and ferrosilite (Fs, $Fe_2Si_2O_6$) (**Fig. 3A**). Some regions in the single large poikilitic augite grain investigated have small variations in Ca (<0.7 wt% Ca), Fe (<0.6 wt%), Mg (<0.6 wt) and Cl (~0.3 wt%) (**Table S3**) that could indicate the presence of inclusions, thin lamellae of pyroxene of different compositions and/or minor alteration products that are smaller than PIXL's x-ray beam size. Fe/Mn ratios of olivine and pyroxene in meteorites have been used to determine their planetary parentage (*19*). The molar Fe/Mn ratios of olivine and pyroxene in Martian meteorites are 47 ± 3 and 32 ± 6 (1 standard deviation), respectively (*19*). The Dourbes minerals have ranges of molar Fe/Mn ratios of 55 ± 8 to 67 ± 9 for olivine and 38 ± 13 to 42 ± 3, for augite. The lower ends of these ranges are consistent with the values found for meteorites; we speculate that the higher Fe/Mn values could be due to a small amount of Fe-bearing minerals formed from aqueous alteration of olivine.

Mesostasis areas show few signs of secondary salts; they have low abundances of SO_3 and Cl and all analyzed element abundances sum to ~94.0 – 99.5 wt% (**Table S4**), indicating the presence of little-to-no additional material enriched in C or H, which PIXL cannot detect directly. Compositions of the Fe-Cr-Ti oxide grains in Dourbes vary, depending on their petrographic setting. Those embedded in olivine have high molar Cr/Ti (~10), those at olivine-pyroxene boundaries have moderate Cr/Ti (~3.6), and those in mesostasis have low Cr/Ti (1-1.9, **Fig. S6**), leading to the variations in their estimated chemistry (**Table S4**). Calcium phosphate occurs only in the mesostasis and has molar Ca/P ratios most consistent with merrillite (9:7) (**Fig. S7**).

Interpretation as an igneous cumulate

We use our observations to evaluate the above hypotheses of the origin of olivine-carbonate unit exposed in Seitah.

Volcaniclastic (e.g., pyroclastic deposits) or impact clastic (e.g., rock fragments cemented by quenched impact melt) origins typically produce heterogeneous mixtures of mineral grains and rock fragments, embedded in a fine-grained matrix of (or altered from) ash particles (<50 μm). For Brac and Bastide outcrops in the Séítah formation, there is no evidence of rock fragments or a zoned fine-grained texture (**Fig. 1**). Observations of other outcrops also reveal no evidence of heterogeneous mixtures (*5*). We therefore exclude this possibility.

Sedimentary deposition of detrital olivine grains with cements is unlikely. The observed assemblage of coarse-grain augite and mesostasis with feldspar and Fe-Cr-Ti oxides has not previously been observed as a sedimentary cement, and would not precipitate from fluids at near-surface temperatures and pressures. These grains are also too coarsely crystalline to be a detrital

matrix. It is also not likely that the entire abrasion patch sits within one rock fragment in an extremely coarse-grained water-transported clastic rock (i.e., a conglomerate), because there is no evidence in images of the host rock for pebble-sized or larger grain boundaries, cements or fine-grained matrix, hydraulic sorting, sedimentary structures, erosion, or channel forms, as would be expected for such a deposit (*5*).

Instead, we conclude that the olivine and augite formed by cooling of a magma body. The magma could have arisen from volcanism or an impact, because impact melting can fully homogenize the target rock, which would then solidify and crystalize very similarly to a volcanic magma originating from the Martian mantle. We interpret Brac to be a cumulate igneous rock formed by settling and accumulation of olivine crystals from a molten mafic magma. The observed poikilitic texture is common in cumulate rocks on Earth (*20*) and in several Martian meteorites (*21*). The compositional trend in Cr/Ti ratios we observed in the Fe-Cr-Ti oxide grains is also consistent with oxides crystallizing from a cooling magma (**Fig. S6**). The similarity in mineralogy (*5*), textures, color, and reflectance spectral properties between Brac and Bastide within the Séítah formation indicates that our cumulate lithology interpretation can be extrapolated beyond the Dourbes abraded patch.

Petrogenetic history

We next consider the magmatic crystallization and cooling history of the olivine cumulate outcrops in the Séítah formation. Using the chemistry of the olivine (**Fig. S5)**, we infer that the magma was more iron rich (Mg# = 27 to 30; Mg# is molar Mg/(Mg+Fe) × 100) *(16)*, than previously found (Mg# = 52 to 67) for Martian meteorites (*22*, *23*). We suggest that Séítah cumulate rocks formed from a parent magma that had previously lost Mg-rich minerals. Brac is different in both mineralogy and bulk chemistry from olivine-rich cumulates in Martian meteorites, and also from olivine-rich rocks at Gusev crater investigated by the Spirit rover (**Figs. 3 and 4A**) *(16)*. The olivine grain size distribution and uniform composition in Brac, as well as the lack of larger olivine crystals observed in any Séítah outcrops, indicates an initially crystal-free melt (**Fig. 5B**). The presence of similar sized olivine grains indicates an early stage of rapid homogeneous olivine nucleation, due to oversaturation, possibly induced by rapid cooling (**Fig. 5C**). Additionally, the presence of melt inclusions (typically 100-300 μm, with one up to ~600 μm) in the Dourbes olivine grains (**Figs. 2D and S4**) suggests early rapid growth of olivine, forming crystals with open space between their outside faces (hopper or skeletal shaped crystals), typical morphology under rapid cooling (*24*). Later, olivine crystal of euhedral shapes formed through additional olivine growth filling in the open space, before or during gravitational settling (**Fig. 5C**). The gravitational settling forms a framework of olivine grains of mostly point contact with open space between grains (**Fig. 5D**). There is little textural or chemical evidence for later olivine growth filling in the open space, indicating that the cumulate was unaffected by subsequent magma infiltration or exchange after the olivine crystals had formed and accumulated. The proportion (~35 vol%) of other minerals among the olivine is consistent with the expected porosity of an olivine cumulate unaffected by compaction (*25*). The chemical equilibrium of olivine and augite and the coarse grains of augite implies extended cooling at a temperature (~1085 ºC) below that olivine starts to crystallize *(16)*.

Emplacement history

Olivine cumulates can form in different geological settings, including large layered mafic intrusions (LLMIs), thick lava flows/ponds, shallow intrusive bodies as sills/laccoliths, or thick melt sheets from large impacts or their melt ejecta (**Fig. 5A**). The emplacement environment of

cumulate rocks as observed in the Séítah formation can be assessed using Earth analogs, after considering the difference in gravity *(16)*. Unlike similar rocks in Earth LLMIs (*20*), Séítah olivine grains host large melt inclusions and show negligible additional growth after the olivine framework formed, indicating that Brac formed at depths of no more than a few kilometers. Thick (100-150 m) mafic or ultramafic lava flows or ponds on Earth form uncompacted frameworks of euhedral to subhedral olivine, similar to those observed in the Séítah formation. However, among Earth examples, olivine grains are typically smaller and the mesostasis is more fine-grained (or glassy) than in Séítah rocks *(16).* This indicates that these Martian cumulates experienced later cooling at a lower rate than Earth analogs. We suggest potential explanations of a thicker lava than on Earth; or emplacement into hot surroundings (e.g. a crystal laden lava injecting into a still-hot flow); or an intrusive environment such as a sill or a laccolith (a lens-shaped igneous formation). Alternatively, similar features could have formed in a super-heated impact melt sheet.

In those environments, olivine cumulates represent only the lower portion of the petrogenetic sequence. On Earth, pyroxene-rich cumulates commonly occur stratigraphically above olivine-rich layers, with a trend of minerals increasing in Fe, Na, and K higher in the sequence (**Fig. 5D**). Similar petrogenetic sequences have been hypothesized for cumulate Martian meteorites (*26–28*). The overlying Máaz formation could consist of such rocks (*5*); however, the contact between the Séítah and Máaz formations is obscured along the rover traverse, preventing a definitive determination of their relationship *(5)*. Alternatively, the originally overlying strata might not have been explored by the rover; could have been eroded; or there is no petrographic link between the Séítah and Máaz formations.

Regional and Planetary Context

The presence of olivine cumulates in Jezero crater constrains the origin of the more widespread olivine-bearing regional units in Isidis Planitia. On petrologic evidence alone, it is most plausible that emplacement of the Séítah olivine cumulate was by magma injection into an environment that permitted slow cooling, such as a shallow igneous intrusion in the Martian crust or into existing lava flows (*6*). However, this interpretation does not necessarily extend to the regional scale. A single large shallow intrusion seems unlikely to explain a regional unit over such a wide (>70,000 km^2) area with diverse local topographical influences. Similarly, the cumulate rock does not support the hypothesis that the regional unit is formed by a single deposit of clastic material (volcanic ash, impact ash or sediments). We suggest that the regional exposure represents a series of related intrusive (sills, laccoliths) and extrusive magma bodies (lava flows, pyroclastic deposits). It could also contain some reworked sedimentary derivatives of the igneous rocks.

Abundances of incompatible elements, i.e., those that preferentially partition in the melt (e.g., Na, K, Rb, Sr, La, Sm, Nd, Yb, U, Th), in igneous rocks constrain the mantle source compositions. Ratios of rare earth elements (e.g, La/Yb) are often used. However, these elements are of low abundances (typically at parts per million or parts per billion by weight) that are below PIXL's ability to detect. Instead, the abundance ratio of K_2O/TiO_2 can be used to constrain source characteristics, provided the magma has not experienced crystallization and removal of K- or Ti-bearing minerals (*29*). We compare our results to meteorites and igneous rocks studied by other rovers. The weight K_2O/TiO_2 ratio (0.38 ± 0.48) of the unaltered portion of Dourbes plots in the range shown by Martian meteorites containing olivine cumulates (chassignite) or augite cumulates (nakhlite), as well as mafic rocks investigated by other Mars rovers and landers (**Fig. 4B**). All these samples are enriched in highly incompatible elements

(e.g., K, U, and Th) compared to Ti (*30*). Measurements of samarium-neodymium and rubidium-strontium isotopes in nakhlites and chassignites indicated that their mantle sources were depleted in highly incompatible elements; this suggests enrichment of highly incompatible elements in these cumulate meteorites during melt separation from the mantle sources (*26*, *28*). Process to enrich highly incompatible elements, possibly driven by interaction with high-temperature aqueous fluids after rock formation (metasomatic processes), has previously been suggested for the mantle source regions of meteorites (*31*), alkali-rich basalts in Gusev crater (*32*) and Gale crater (*33*, *34*). Alternatively, geophysical data and models have been interpreted as indicating that Mars' mantle is depleted overall in heat producing (K, U, Th) and other highly incompatible elements, implying that those elements are instead concentrated in the planet's crust or upper mantle (*35*). Elevated abundances of highly incompatible elements in the mantle source regions at Gusev, Gale, and Jezero craters, as well as those for chassignites and nakhlites (*31*), could indicate a general enrichment of such elements in Mars' upper mantle, possibly caused by metasomatic processes and/or plume activity. These different samples range from a formation age of > 3.9 Ga to 1.34 Ga (*3, 36*). This wide range of ages and geographic locations of igneous rocks with these properties indicate a long-lived process that has been operating on Mars for billions of years and has affected a large fraction of Mars's crust and upper mantle (*16*).

References and Notes

1. S. C. Werner, The early martian evolution—Constraints from basin formation ages. *Icarus*. **195**, 45–60 (2008).

2. L. Mandon et al., Refining the age, emplacement and alteration scenarios of the olivine-rich unit in the Nili Fossae region, Mars. *Icarus*. **336**, 113436 (2020).

3. B. L. Ehlmann *et al.*, Orbital Identification of Carbonate-Bearing Rocks on Mars. *Science* **322**, 1828 (2008).

4. A. J. Brown, C. E. Viviano, T. A. Goudge, Olivine-carbonate mineralogy of the Jezero Crater region. *J. Geophys. Res. Planets*. **125**, e2019JE006011 (2020), doi:https://doi.org/10.1029/2019JE006011.

5. K. A. Farley et al., Aqueously altered igneous rocks on the floor of Jezero crater, Mars. *Science (this issue).*

6. T. M. Hoefen, R. N. Clark, J. L. Bandfield, M. D. Smith, J. C. Pearl, P. R. Christensen, Discovery of olivine in the Nili Fossae Region of Mars. *Science.* **302**, 627–630 (2003).

7. M. S. Bramble, J. F. Mustard, M. R. Salvatore, The geological history of Northeast Syrtis Major, Mars. *Icarus*. **293**, 66–93 (2017).

8. B. L. Ehlmann, J. F. Mustard, An in-situ record of major environmental transitions on early Mars at Northeast Syrtis Major. *Geophys. Res. Lett.* **39**, 1–7 (2012).

9. L. L. Tornabene, J. E. Moersch, H. Y. McSween Jr., V. E. Hamilton, J. L. Piatek, P. R. Christensen, Surface and crater-exposed lithologic units of the Isidis Basin as mapped by coanalysis of THEMIS and TES derived data products. *J. Geophys. Res. Planets*. **113** (2008), doi:https://doi.org/10.1029/2007JE002988.

10. J. L. Bishop et al., Mineralogy and morphology of geologic units at Libya Montes, Mars: Ancient

aqueously derived outcrops, mafic flows, fluvial features, and impacts. *J. Geophys. Res. Planets*. **118**, 487–513 (2013).

11. A. Ody, F. Poulet, J.-P. Bibring, D. Loizeau, J. Carter, B. Gondet, Y. Langevin, Global investigation of olivine on Mars: Insights into crust and mantle compositions. *J. Geophys. Res. Planets*. **118**, 234–262 (2013).

12. V. E. Hamilton, P. R. Christensen, Evidence for extensive, olivine-rich bedrock on Mars. *Geology*. **33**, 433–436 (2005).

13. C. H. Kremer, J. F. Mustard, M. S. Bramble, A widespread olivine-rich ash deposit on Mars. *Geology*. **47**, 677–681 (2019).

14. A. D. Rogers, N. H. Warner, M. P. Golombek, J. W. Head III, J. C. Cowart, Areally extensive surface bedrock exposures on Mars: Many are clastic rocks, not lavas. *Geophys. Res. Lett.* **45**, 1767–1777 (2018).

15. A. C. Allwood et al., PIXL : planetary instrument for x-ray lithochemistry. *Space Sci. Rev.* **216** (2020), doi:10.1007/s11214-020-00767-7.

16. See upplementary materials.

17. N. Morimoto *et al.*, Nomenclature of pyroxenes. *American Mineralogist* **73**, 1123-1133 (1988).

18. R. W. Le Maitre et al., *Igneous rocks: a classification and glossary of terms* (Cambridge University Press, Cambridge, United Kingdom, Second., 2002).

19. J. J. Papike, J. M. Karner, J. M. Shearer, Determination of planetary basalt parentage: A simple technique using the electron microprobe. *Am. Mineral.* **88**, 469–472 (2003).

20. L. R. Wager, The major element variation of the layered series of the Skaergaard intrusion and a re-estimation of the average composition of the hidden layered series and of the successive residual magmas. *J. Petrol.* **1**, 364–398 (1960).

21. R. R. Rahib et al., Mantle source to near-surface emplacement of enriched and intermediate poikilitic shergottites in Mars. *Geochim. Cosmochim. Acta*. **266**, 463–496 (2019).

22. D. S. Musselwhite, H. A. Dalton, W. S. Kiefer, A. H. Treiman, Experimental petrology of the basaltic shergottite Yamato-980459: Implications for the thermal structure of the martian mantle. *Meteorit. Planet. Sci. Arch.* **41**, 1271–1290 (2005).

23. J. B. Balta, H. Y. McSween, Water and the composition of martian magmas. *Geology*. **41**, 1115–1118 (2013).

24. F. Faure, P. Schiano, G. Trolliard, C. Nicollet, B. Soulestin, Textural evolution of polyhedral olivine experiencing rapid cooling rates. *Contrib. to Mineral. Petrol.* **153**, 405–416 (2007).

25. M. W. Schmidt, M. Forien, G. Solferino, N. Bagdassarov, Settling and compaction of olivine in basaltic magmas: an experimental study on the time scales of cumulate formation. *Contrib. to Mineral. Petrol.* **164**, 959–976 (2012).

26. A. H. Treiman, The nakhlite meteorites: Augite-rich igneous rocks from Mars. *Chemie der Erde*. **65**,

203–270 (2005).

27. F. M. McCubbin, S. M. Elardo, C. K. Shearer, A. Smirnov, E. H. Hauri, D. S. Draper, A petrogenetic model for the comagmatic origin of chassignites and nakhlites: Inferences from chlorine-rich minerals, petrology, and geochemistry. *Meteorit. Planet. Sci.* **48**, 819–853 (2013). (apatite source)

28. A. Udry, J. M. D. Day, 1.34 billion-year-old magmatism on Mars evaluated from the co-genetic nakhlite and chassignite meteorites. *Geochim. Cosmochim. Acta*. **238**, 292–315 (2018).

29. M. E. Schmidt, C. M. Schrader, T. J. McCoy, The primary fO_2 of basalts examined by the Spirit rover in Gusev Crater, Mars: Evidence for multiple redox states in the martian interior. *Earth Planet. Sci. Lett.* **384**, 198–208 (2013).

30. A. H. Treiman, Chemical compositions of martian basalts (shergottites): some inferences on basalt formation, mantle metasomatism, and differentiation on Mars. *Meteorit. Planet. Sci.* **38**, 1849–1864 (2003).

31. J. M. D. Day *et al.*, Martian magmatism from plume metasomatized mantle. *Nature Communications* **9**, 4799 (2018).

32. M. E. Schmidt, T. J. McCoy, The evolution of a heterogeneous Martian mantle: Clues from K, P, Ti, Cr, and Ni variations in Gusev basalts and shergottite meteorites. *Earth Planet. Sci. Lett.* **296**, 67–77 (2010).

33. E. M. Stolper et al., The petrochemistry of Jake M: A martian mugearite. *Science.* **341**, 1239463 (2013).

34. M. E. Schmidt et al., Geochemical diversity in first rocks examined by the Curiosity Rover in Gale Crater: Evidence for and significance of an alkali and volatile-rich igneous source. *J. Geophys. Res. Planets*. **119**, 64–81 (2014).

35. G. J. Taylor et al.., Bulk composition and early differentiation of Mars. *J. Geophys. Res. Planets*. **111** (2006), doi:https://doi.org/10.1029/2005JE002645.

36. L. E. Nyquist *et al.*, Ages and geologic histories of Martian meteorites. *Space Science Reviews* **96**, 105-164 (2001).

37. M. J. Le Bas, R. W. Le Maitre, A. Streckeisen, B. Zanettin, A chemical classification of volcanic rocks based on the total alkali–silica diagram. *Journal of Petrology* **27**, 745-750 (1986).

38. A. R. Santos *et al.*, Petrology of igneous clasts in Northwest Africa 7034: Implications for the petrologic diversity of the martian crust. *Geochim. Cosmochim. Acta* **157**, 56-85 (2015).

39. R. C. Moeller et al., The sampling and caching subsystem (SCS) for the scientific exploration of Jezero Crater by the Mars 2020 Perseverance rover. *Space Sci. Rev.* **217**, 5 (2020).

40. D. A. K. Pedersen, J. Henneke, J. L. Jørgensen, Y. Liu, J. . Hurowitz, in *52nd Lunar and Planetary Science Conference*, Abstract #1198 presented at the 52nd Lunar and Planetary Science Conference (2021).

41. C. M. Heirweghet al., Abstract #1260 presented at the 52nd Lunar and Planetary Science Conference (2021).

42. W. Nikonow, D. Rammlmair, Risk and benefit of diffraction in energy dispersive x-ray fluorescence mapping. *Spectrochim. Acta B*. **125**, 120–126 (2016).

43. C. A. Schneider, W. S. Rasband, K. W. Eliceiri, NIH Image to ImageJ: 25 years of image analysis. *Nat. Methods*. **9**, 671–675 (2012).

44. R. R. Loucks, A precise olivine-augite Mg-Fe-exchange geothermometer. *Contrib. to Mineral. Petrol.* **125**, 140–150 (1996).

45. C. K. Shearer, P. V. Burger, J. J. Papike, F. M. McCubbin, A. S. Bell, Crystal chemistry of merrillite from Martian meteorites: Mineralogical recorders of magmatic processes and planetary differentiation. *Meteorit. Planet. Sci.* **50**, 649–673 (2015). Figure S7 merrillite source

46. A. Udry, G. H. Howarth, C. D. K. Herd, J. M. D. Day, T. J. Lapen, J. Filiberto, What martian meteorites reveal about the interior and surface of Mars. *J. Geophys. Res. Planets*. **125**, 1–34 (2020).

47. J. Filiberto, J. Gross, J. Trela, E. Ferré, Gabbroic Shergottite Northwest Africa 6963: An intrusive sample of Mars. *Am. Mineral.* **99**, 601–606 (2014).

48. T. V. Kizovski, K. T. Tait, V. E. Di Cecco, L. F. White, D. E. Moser, Detailed mineralogy and petrology of highly shocked poikilitic shergottite Northwest Africa 6342. *Meteorit. Planet. Sci.* **54** (2019), doi:10.1111/maps.13255.

49. G. H. Howarth, J. F. Pernet-Fisher, J. B. Balta, P. H. Barry, R. J. Bodnar, L. A. Taylor, Two-stage polybaric formation of the new enriched, pyroxene-oikocrystic, lherzolitic shergottite, NWA 7397. *Meteorit. Planet. Sci.* **49**, 1812–1830 (2014).

50. J. Gattacceca et al., The Meteoritical Bulletin, no. 109. *Meteorit. Planet. Sci.* **56**, 1626–1630 (2021).

51. R. H. Hewins et al.et al., Northwest Africa 8694, a ferroan chassignite: Bridging the gap between nakhlites and chassignites. *Geochim. Cosmochim. Acta*. **282**, 201–226 (2020).

52. H. Y. McSween et al., Alkaline volcanic rocks from the Columbia Hills, Gusev crater, Mars. *J. Geophys. Res. E Planets*. **111**, 1–15 (2006).

53. J. Zipfel, C. Schroeder, B. L. Jolliff, R. Gellert, K. E. Herkenhoff, R. Rieder, R. Anderson, J. F. Bell III, J. Brueckner, J. A. Crisp, Bounce Rock—A shergottite-like basalt encountered at Meridiani Planum, Mars. *Meteorit. Planet. Sci.* **46**, 1–20 (2011).

54. A. Cousin, V. Sautter, V. Payré, O. Forni, N. Mangold, O. Gasnault, L. Le Deit, J. Johnson, S. Maurice, M. Salvatore, R. C. Wiens, P. Gasda, W. Rapin, Classification of igneous rocks analyzed by ChemCam at Gale crater, Mars. *Icarus*. **288**, 265–283 (2017).

55. D. W. Ming et al., Geochemical and mineralogical indicators for aqueous processes in the Columbia Hills of Gusev crater, Mars. *J. Geophys. Res. E Planets*. **111** (2006), doi:10.1029/2005JE002560.

56. R. V. Morris et al., Identification of carbonate-rich outcrops on Mars by the spirit rover. *Science.* **329**, 421–424 (2010).

57. R. A. Yingst, D. W. Schmidt, M.E., Herkenhoff, K.E. Mittlefehldt, Abstract #3296 presented at the 7th International Conference on Mars (2007).

58. D. W. Mittlefehldt, R. Gellert, T. McCoy, H. Y. McSween, R. Li, Abtract #1505 presented at the 37th Lunar and Planetary Science Conference (2006).

59. M. C. Johnson, M. J. Rutherford, P. Hess, Chassigny petrogenesis: Melt compositions, intensive parameters and water contents of martian magmas. *Geochim. Cosmochim. Acta*. **55**, 349–366 (1991).

60. Q. He, L. Xiao, W. Hsu, B. Balta, H. Y. McSween, Y. Liu, The water content and parental magma of the second chassignite NWA 2737: Clues from trapped melt inclusions in olivine. *Meteorit. Planet. Sci.* (2013).

61. L. V. Danyushevsky, F. N. Della-Pasqua, S. Sokolov, Re-equilibration of melt inclusions trapped by magnesian olivine phenocrysts from subduction-related magmas: petrological implications. *Contrib. to Mineral. Petrol.* **138**, 68–83 (2000).

62. J. Longhi, Complex magmatic processes on Mars - Inferences from the SNC meteorites. *Proc. Lunar Planet. Sci.* **21** (1991).

63. M. E. Minitti, M. J. Rutherford, Genesis of the Mars Pathfinder "sulfur-free" rock from SNC parental liquids. *Geochim. Cosmochim. Acta*. **64**, 2535–2547 (2000).

64. J. Filiberto, Experimental constraints on the parental liquid of the chassigny meteorite: a possible link between the chassigny meteorite and a Gusev basalt. *Geochim. Cosmochim. Acta*. **72**, 690–701 (2008).

65. K. R. Stockstill, H. Y. McSween Jr., R. J. Bodnar, Melt inclusions in augite of the Nakhla martian meteorite: Evidence for basaltic parental melt. *Meteorit. Planet. Sci.* **40**, 377 (2005).

66. R. C. F. Lentz, T. J. McCoy, L. E. Collins, C. M. Corrigan, G. K. Benedix, G. J. Taylor, R. P. Harvey, Theo's Flow, Ontario, Canada: A terrestrial analog for the martian nakhlite meteorites. *Analogs for Planetary Exploration*. **483** (2011).

67. D. R. Pyke, A. J. Naldrett, O. R. Eckstrand, Archean ultramafic flows in Munro Township, Ontario. *GSA Bull.* **84**, 955–978 (1973).

68. N. T. Arndt, A. J. Naldrett, D. R. Pyke, Komatiitic and iron-rich tholeiitic lavas of Munro Township, Northeast Ontario. *J. Petrol.* **18**, 319–369 (1977).

69. W. E. Stone, L. S. Jensen, W. R. Church, Petrography and geochemistry of an unusual Fe-rich basaltic komatiite from Boston Township, Northeastern Ontario. *Can. J. Earth Sci.* **24**, 2537–2550 (1987).

70. W. E. Stone, J. H. Crocket, A. P. Dickin, M. E. Fleet, Origin of Archean ferropicrites: geochemical constraints from the Boston Creek flow, Abitibi greenstone belt, Ontario, Canada. *Chem. Geol.* **121**, 51–71 (1995).

71. M. Murri, M. C. Domeneghetti, A. M. Fioretti, F. Nestola, F. Vetere, D. Perugini, A. Pisello, M. Faccenda, M. Alvaro, Cooling history and emplacement of a pyroxenitic lava as proxy for understanding Martian lava flows. *Sci. Rep.* **9**, 17051 (2019).

72. J. C. Dann, T. L. Grove, in *Developments in Precambrian Geology,* M. J. van Kranendonk, R. H. Smithies, V. C. Bennett, Eds. (Elsevier, 2007), vol. 15, pp. 527-570.

73. R. T. Helz, Crystallization history of Kilauea Iki lava lake as seen in drill core recovered in 1967-1979. *Bull. Volcanol.* **43**, 675–701 (1980).

74. H. C. Hardee, Solidification in Kilauea Iki lava lake. *J. Volcanol. Geotherm. Res.* **7**, 211–223 (1980).

75. N. Vinet, M. D. Higgins, What can crystal size distributions and olivine compositions tell us about magma solidification processes inside Kilauea Iki lava lake, Hawaii? *J. Volcanol. Geotherm. Res.* **208**, 136–162 (2011).

76. I. S. Puchtel, A. W. Hofmann, V. V Kulikova, Petrology of a 2.41 Ga remarkably fresh komatiitic basalt lava lake in Lion Hills, central Vetreny Belt, Baltic Shield. *Contrib. to Mineral. Petrol.* **124**, 273–290 (1996).

77. N. T. Arndt, Spinifex and swirling olivines in a komatiite lava lake, Munro Township, Canada. *Precambrian Res.* **34**, 139–155 (1986).

78. L. Wilson, J. W. Head III, Mars: Review and analysis of volcanic eruption theory and relationships to observed landforms. *Rev. Geophys*. **32**, 221–263 (1994).

79. J. D. Macdougall, Continental Flood Basalts (Springer Netherlands, Petrology and Structural Geology, 1988).

80. K. Hon, J. Kauahikaua, R. Denlinger, K. Mackay, Emplacement and inflation of pahoehoe sheet flows: Observations and measurements of active lava flows on Kilauea Volcano, Hawaii. *Geological Society of America Bull.* **106**, 351–370 (1994).

81. S. Self, T. Thordarson, L. Keszthelyi, Emplacement of Continental Flood Basalt Lava Flows. *Large Igneous Prov. Cont. Ocean. Planet. Flood Volcanism* (1997), pp. 381–410.

82. S. Self, L. Keszthelyi, T. Thordarson, The Importance of Pahoehoe. Annu. Rev. *Earth Planet. Sci.* **26**, 81–110 (1998).

83. N. E. Moore, A. L. Grunder, W. A. Bohrson, The three-stage petrochemical evolution of the Steens Basalt (southeast Oregon, USA) compared to large igneous provinces and layered mafic intrusions. *Geosphere.* **14**, 2505–2532 (2018).

84. N. Arndt, C. M. Lesher, S. J. Barnes, Komatiite (Cambridge University Press, Cambridge, 2008).

85. J. M. Husch, Palisades sill: Origin of the olivine zone by separate magmatic injection rather than gravity settling. *Geology.* **18**, 699–702 (1990).

86. W. D. Smith, W. Maier, The geotectonic setting, age and mineral deposit inventory of global layered intrusions. *Earth-Science Rev.* **220** (2021).

87. O. Namur et al., Igneous layering in basaltic magma chambers. *Layered intrusions*, 75–152 (2015).

88. H. V. Eales, R. G. Cawthorn, The bushveld complex. *Dev. Petrol.* **15**, 181–229 (1996).

89. T. B. Grant et al.., Anatomy of a deep crustal volcanic conduit system; the Reinfjord ultramafic complex, Seiland Igneous Province, northern Norway. *Lithos*. **252**, 200–215 (2016).

90. J. Filiberto, R. Dasgupta, Fe^{2+}-Mg partitioning between olivine and basaltic melts: Applications to genesis of olivine-phyric shergottites and conditions of melting in the Martian interior. *Earth Planet.*

Sci. Lett. **304**, 527–537 (2011).

91. Y. Liu, C. Ma, J. R. Beckett, Y. Chen, Y. Guan, Rare-earth-element minerals in martian breccia meteorites NWA 7034 and 7533: Implications for fluid–rock interaction in the martian crust. *Earth Planet. Sci. Lett.* **451**, 251–262 (2016).

92. H. Y. McSween, G. J. Taylor, M. B. Wyatt, Elemental Composition of the Martian Crust. *Science.* **324**, 736–739 (2009).

93. R. H. Hewins, B. Zanda, M. Humayun, A. Nemchin, J. P. Lorand, S. Pont, et al., Regolith breccia Northwest Africa 7533: Mineralogy and petrology with implications for early Mars. *Meteorit. Planet. Sci.* **52**, 89–124 (2017).

94. M. E. Schmidt, M. R. M. Izawa, A. P. Thomas, L. M. Thompson, R. Gellert, Abstract #1571 presented at the 48th Lunar and Planetary Science Conference (2017).

95. J. A. Berger, R. Gellert, N. I. Boyd, P. L. King, M. A. McCraig, C. D. O'Connell-Cooper, et al., Elemental composition and chemical evolution of geologic materials in Gale Crater, Mars: APXS results From Bradbury Landing to the Vera Rubin Ridge. *J. Geophys. Res. Planets.* **125**, e2020JE006536 (2020), doi:https://doi.org/10.1029/2020JE006536.

96. R. Gellert, R. Rieder, J. Brückner, B. C. Clark, G. Dreibus, G. Klingelhöfer, et al., Alpha Particle X-Ray Spectrometer (APXS): Results from Gusev crater and calibration report. *J. Geophys. Res. Planets*. **111** (2006), doi:https://doi.org/10.1029/2005JE002555.

97. D. W. Ming, R. Gellert, R. V. Morris, R. E. Arvidson, J. Brückner, B. C. Clark, et al., Geochemical properties of rocks and soils in Gusev Crater, Mars: Results of the Alpha Particle X-Ray Spectrometer from Cumberland Ridge to Home Plate. *J. Geophys. Res. Planets*. **113** (2008), doi:https://doi.org/10.1029/2008JE003195.

98. D. E. Smith *et al.*, Mars Orbiter Laser Altimeter: Experiment summary after the first year of global mapping of Mars. *Journal of Geophysical Research: Planets* **106**, 23689-23722 (2001).

99. J. L. Dickson, L. A. Kerber, C. I. Fassett, B. L. Ehlmann, paper presented at the 49th Annual Lunar and Planetary Science Conference (2018).

100. J. F. Bell *et al.*, The Mars 2020 Perseverance Rover Mast Camera Zoom (Mastcam-Z) Multispectral, Stereoscopic Imaging Investigation. *Space Science Reviews* **217**, 24 (2021).

101. R. Bhartia, L. W. Beegle, L. DeFlores, W. Abbey, J. Razzell Hollis, K. Uckert, et al., Perseverance's scanning habitable environments with raman and luminescence for organics and chemicals (SHERLOC) investigation. *Space Sci. Rev.* **217**, 58 (2021).

102. A.C. Allwood and J.A. Hurowitz, PIXL Raw and Processed Data Bundle (2021), *Planetary Data System; doi:10.17189/1522645*.

103. L. Beegle, Mars 2020 SHERLOC Data Bundle (2021), *Planetary Data System, doi:10.17189/1522643.*

104. J.F. Bell and J.N. Maki, Mast Camera Zoom Data Bundle, from Operations Team, calibrated products (2021), *Planetary Data System, doi:10.17189/BS6B-4782*.

105. W.T. Elam, C.M. Heirwegh PIQUANT Piquant (Version v3.2.11) [Computer software]. Zenodo. https://doi.org/10.5281/zenodo.6959125.

106. S. Davidoff, P. Nemere, T. Barber, A. Galvin, A.P. Wright, S.M. Fedell, R. Stonebraker, J. Corkins (2022), *PIXLISE Core* (Version v2.0) [Computer software]. Zenodo. https://doi.org/10.5281/zenodo.6959096.

107. S. Davidoff, P. Nemere, T. Barber, A. Galvin, A.P. Wright, S.M. Fedell, . Stonebraker, J. Corkins (2022), *PIXLISE UI* (Version v2.0) [Computer software]. Zenodo. https://doi.org/10.5281/zenodo.6959109.

108. S. Davidoff, P. Nemere, T. Barber, A. Galvin, A.P. Wright, S.M. Fedell, R. Stonebraker, J. Corkins (2022), *PIXLISE Diffraction Detection* (Version v2.0) [Computer software]. Zenodo. https://doi.org/10.5281/zenodo.6959138.

109. S. Davidoff, P. Nemere, T. Barber, A. Galvin, A.P. Wright, S.M. Fedell, R.. Stonebraker, J. Corkins (2022), *PIXLISE Data Formats* (Version v2.0) [Computer software]. Zenodo. https://doi.org/10.5281/zenodo.6959146.

Acknowledgments: We are grateful to Mars 2020 team members who participated in tactical and strategic science operations. Detailed comments by K. Edgett are greatly appreciated. YL thank Laszlo P Keszthelyi for the discussion about Earth and Mars lava flows, Nathan Williams for providing the base maps used in Fig. 1A and 1C, and Jim Bell for providing the image used in Fig. 1D.

Funding: The work described in this paper was partially carried out at the Jet Propulsion Laboratory, California Institute of Technology, under a prime contract with the National Aeronautics and Space Administration (80NM0018D0004). YL, MT, ACA, JAH, CMH, SD, RPH, KAF, KMS, JDT, BC, ELC, KM, LWB, LAW, JPG, AHA, BHNH, JRJ, WTE, SMM, AG, RCW, and KU were supported by NASA grant 80NM0018D0004 through JPL. JRJ was also supported by ASU subcontract 15-707. RCW was also supported by NASA grant NNH13ZDA018O for Supercam to LANL. DTF was supported by Australian Research Council grant DE210100205. EAC was supported by Canadian Space Agency grant 19PACOI0 and Natural Sciences and Engineering Research Council of Canada grant RGPIN-2021-02995. CDKH, TVK, and MES were supported by Canadian Space Agency M2020 Participating Scientist grants. AU, SJV, BAC, MN, DLS, JIS, KLS, TBo and BPW were supported by NASA Mars 2020 Participating Scientist grants. The work of KB, SB, OB, LM, NM, CQN, and VS on Mars 2020 was supported by CNES. KHL was supported by a UK Space Agency Aurora Research Fellowship. TBo was supported by the Simons Foundation Collaboration on the Origins of Life. SG was supported by the UK Space Agency and the Royal Society (grant SRF\R1\21000106). AGF was supported by the European Research Council CoG #818602.

Author contributions: YL led the writing of the manuscript. YL, MES, AHT, MMT, JAH, ACA, and TK prepared original draft with input from CDKH, AU, NM, SG, KHL, LM, DLS, DCC, FMM, AJB, JIS, SMM, DOF, CQN, BH. All authors provided input to the manuscript through discussion, editing, or reviewing. YL, MMT, MWMJ, DAKP, JAH, TK, SVB, AK, BCC, BJO involved in methods and data processing. YL, DAKP, JH prepared visualization with contributions from ACA, MES, MWMJ, MMT, CQN, TK, and AHT. KU and YL made Movie S1. Software: WTE and CMH developed PIQUANT; SD led PIXLISE development with PN, AG, and TBa. Project management of PIXL investigation was by ACA as the PIXL principal investigator, JAH as the deputy principal investigator, WTE as the chief spectroscopist, and LAW as the instrument chief engineer.

Competing interests: The Authors declare that they have no competing interests.

Data and materials availability: All data used in this paper are archived in the NASA Planetary Data System (*102-–104*). Image number and data sources for meteorites and rovers used in figures are listed in Table S7. PIXLISE and PIQUANT source codes are are available as open source software (*105-109)*.

Supplementary Materials

Materials and Methods

Supplementary Text

Figs. S1 to S10

Tables S1 to S7

Movie S1

References *(39-109)*

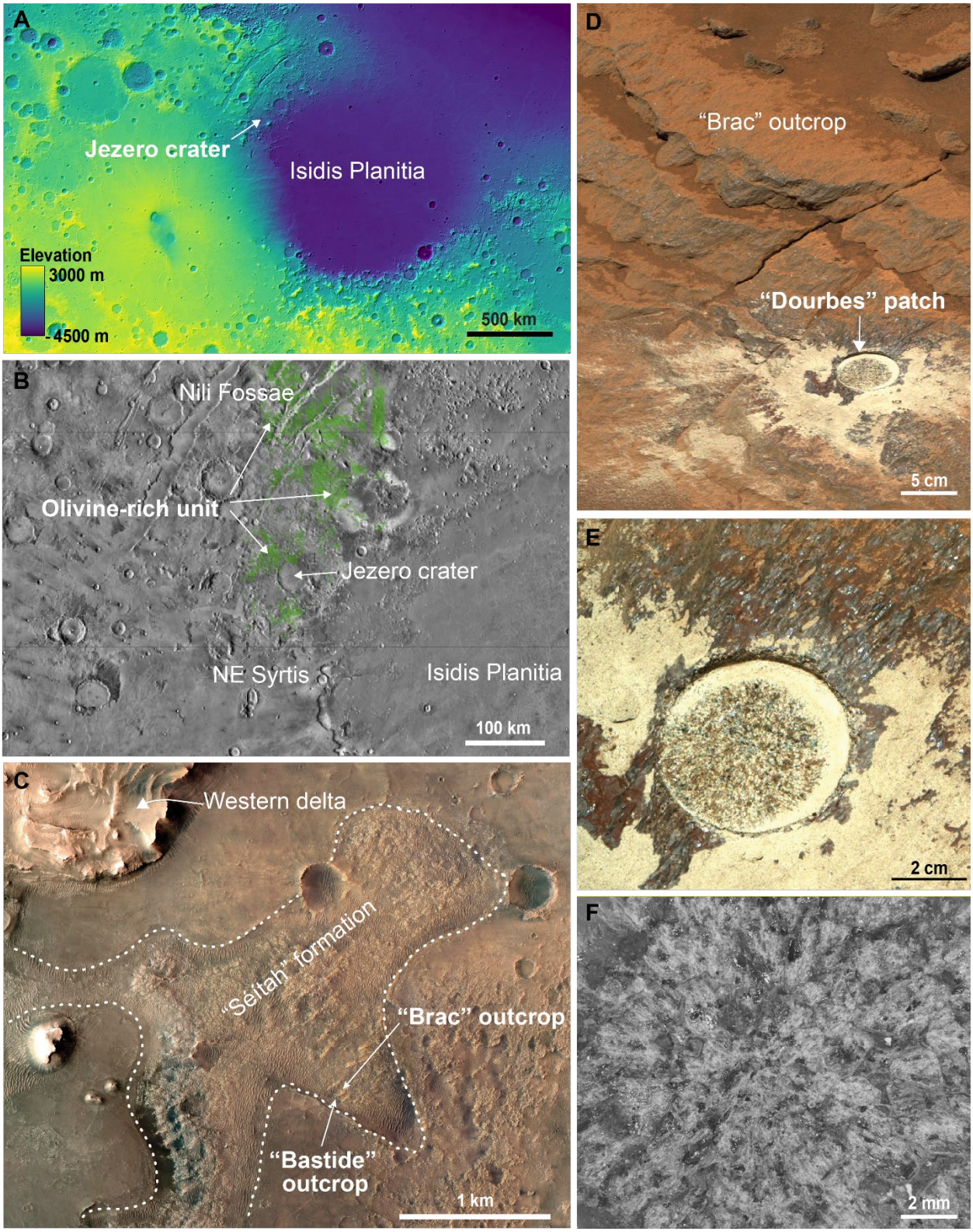

Fig. 1. The Dourbes patch in context from outcrop to regional scale. (A) Colorized terrain topography map showing location of Jezero crater on west edge of Isidis Planitia. Color scale bar shows altitude in meters. (B) Distribution of the regional olivine-bearing unit (green color) on orbital image, data source from (*2*). (C) Color orbital image showing the location of Brac outcrop in the Séítah formation. The dotted white line demarcates the boundary of the Séítah formation

outcrops. (D) Mast Camera Zoom (Mastcam-Z) image of the Brac outcrop, showing 5-10 cm thick layers and the location of Dourbes patch (5 cm diameter). (E) Mastcam-Z image showing more detail of the Dourbes patch. (F) A portion of the abraded patch shown by the autofocus and context imager (ACI) of the Scanning Habitable Environments with Raman and Luminescence for Organics and Chemicals (SHERLOC) instrument on Perseverance rover (*5)*. Image sources are listed in Table S7.

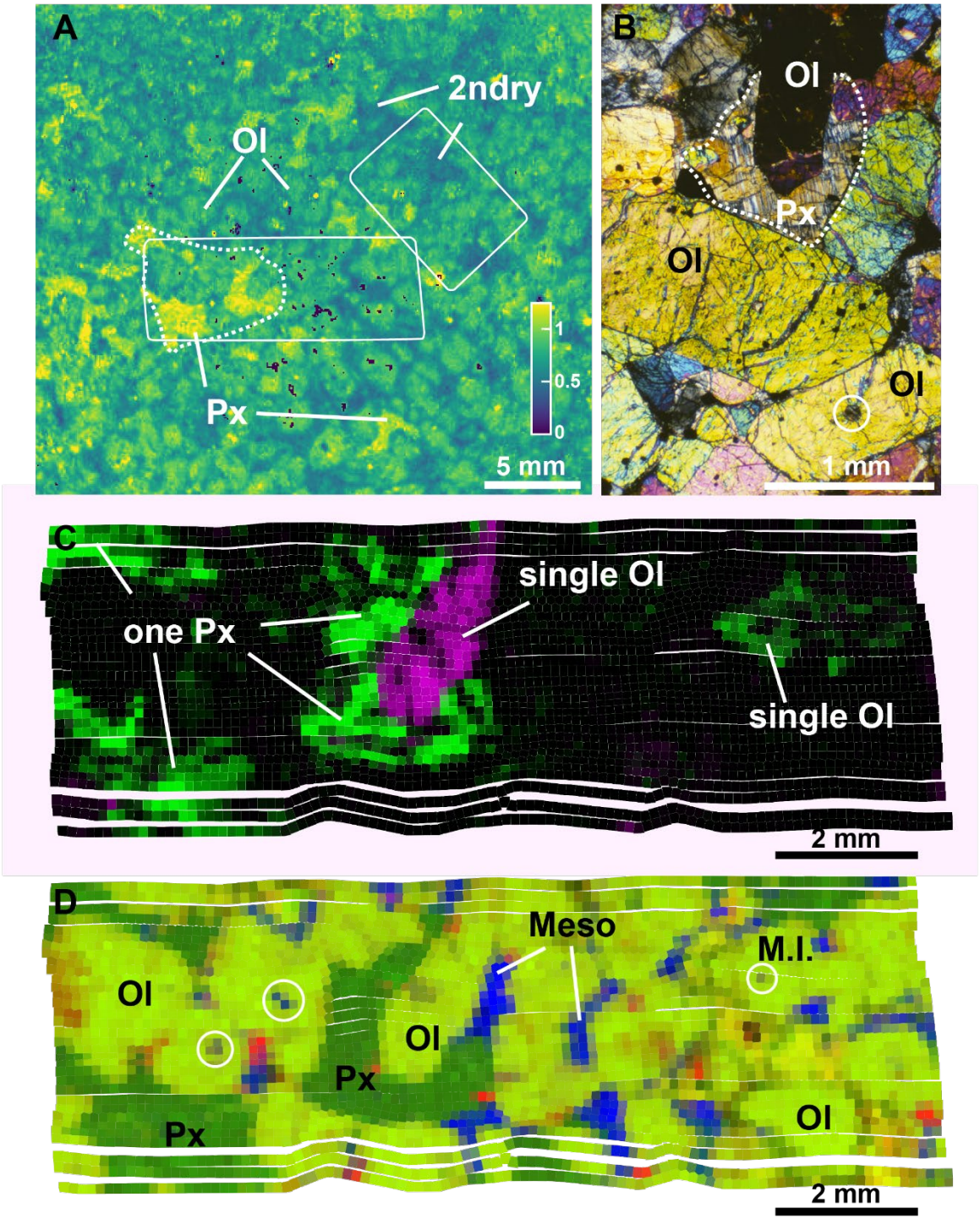

Fig. 2. Cumulate texture of Dourbes. (A) Ratio image taken with the PIXL Micro-Context Camera (MCC), showing the G/NIR ratios (unit shown by the color bar). Dourbes has a cumulate texture with olivine grains (labelled Ol) and a poikilitic texture (region within the white dotted line) with pyroxene (labelled Px). Secondary minerals are labelled as 2ndry. White boxes indicate the areas used for x-ray fluorescence scans (Figs. S3 and S4), the larger of which shown in panels C and D. (B) Cross-polarized light image of the Chassigny meteorite for comparison, showing poikilitic texture. Labels are the same as panel A. The white circle indicates a melt inclusion (M.I.) in Ol. (C) Mineral domain clustering map of the same region shown in panel D.

Green and magenta are used for two different diffraction peaks (7.28 – 7.72 keV and 5.67 – 6.17 keV, respectively). Points with the same diffraction peak are shown in the same color. All three regions of Px chemistry display the same diffraction peak (all green), suggesting these regions are from a single pyroxene crystal. Ol grains inside the Px grains display different orientations although all points inside one grain display the same diffraction peak (magenta) (see Methods in *16*). (D) Chemical map derived from x-ray fluorescence, showing FeO (red), MgO (green), and Al_2O_3 (blue) concentrations. Labels indicate olivine, pyroxenes, and mesostasis (Meso). Blue circles indicate M.I.s (see also Fig. S3 in (*16*) for grayscale images of each element). These composition maps are shown in context with other optical images in Movie S1.

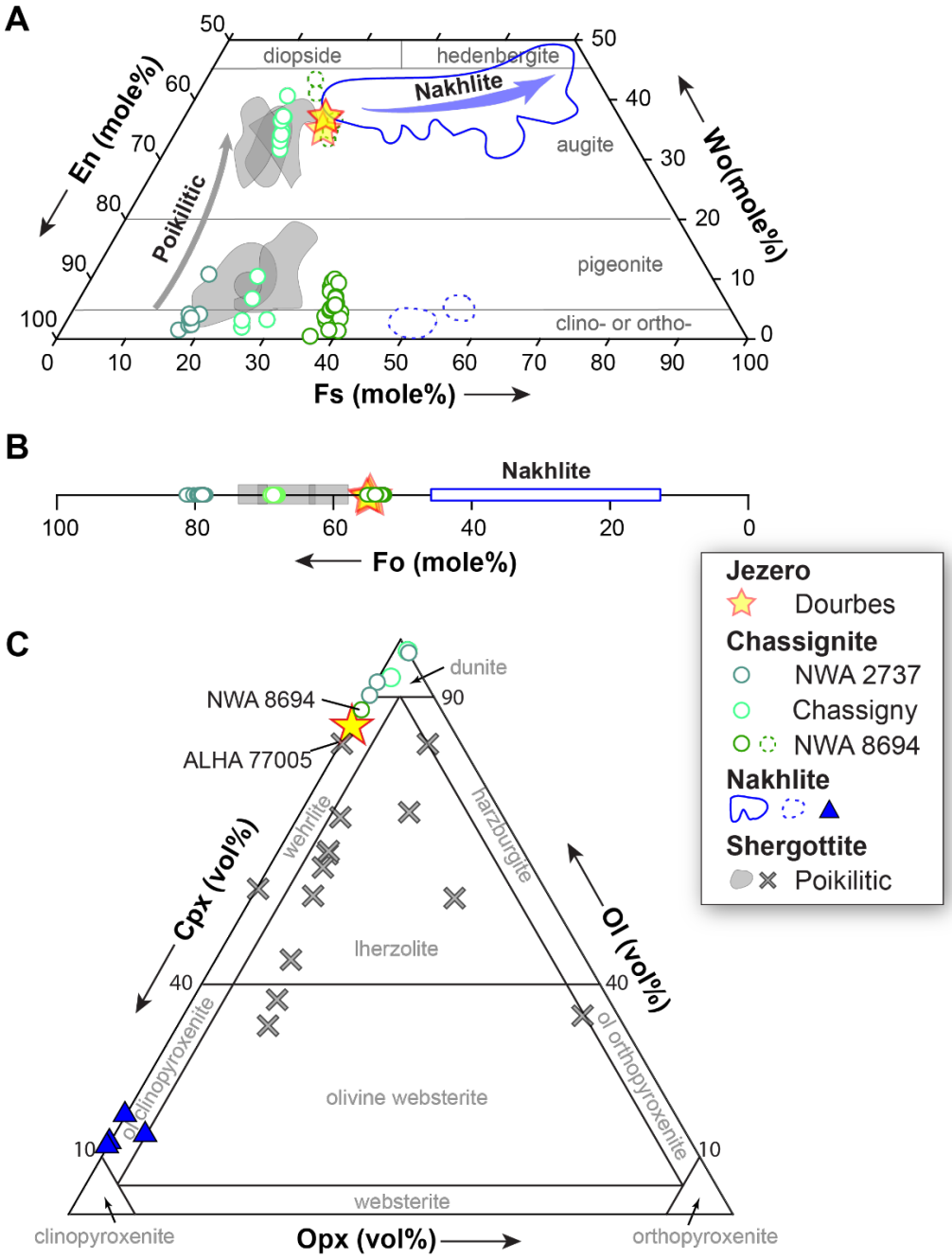

Fig. 3. Mineralogy of Dourbes. (A) Classification of pyroxene using the percentage compositions of wollastonite (Wo), enstatite (En), and ferrosilite (Fs) by (*17*). The average compositions of Dourbes pyroxene grains in Table S3 are shown as star symbols. Symbols or fields with solid lines show volumetrically major pyroxene species and those with dotted blue lines are minor pyroxene species. Arrows show the direction of crystallization. (B) Binary diagram showing mole percentage of forsterite (Fo) in the olivine (Ol). The average compositions of Dourbes olivines (Table S2) are shown as star symbols. Dourbes olivine and pyroxene differ from Martian meteorites. (C) Classification of ultramafic rocks by (*18*) using volume percentages of olivine (Ol), clinopyroxene (Cpx) and orthopyroxene (Opx). Source data for meteorites are listed in Table S7.

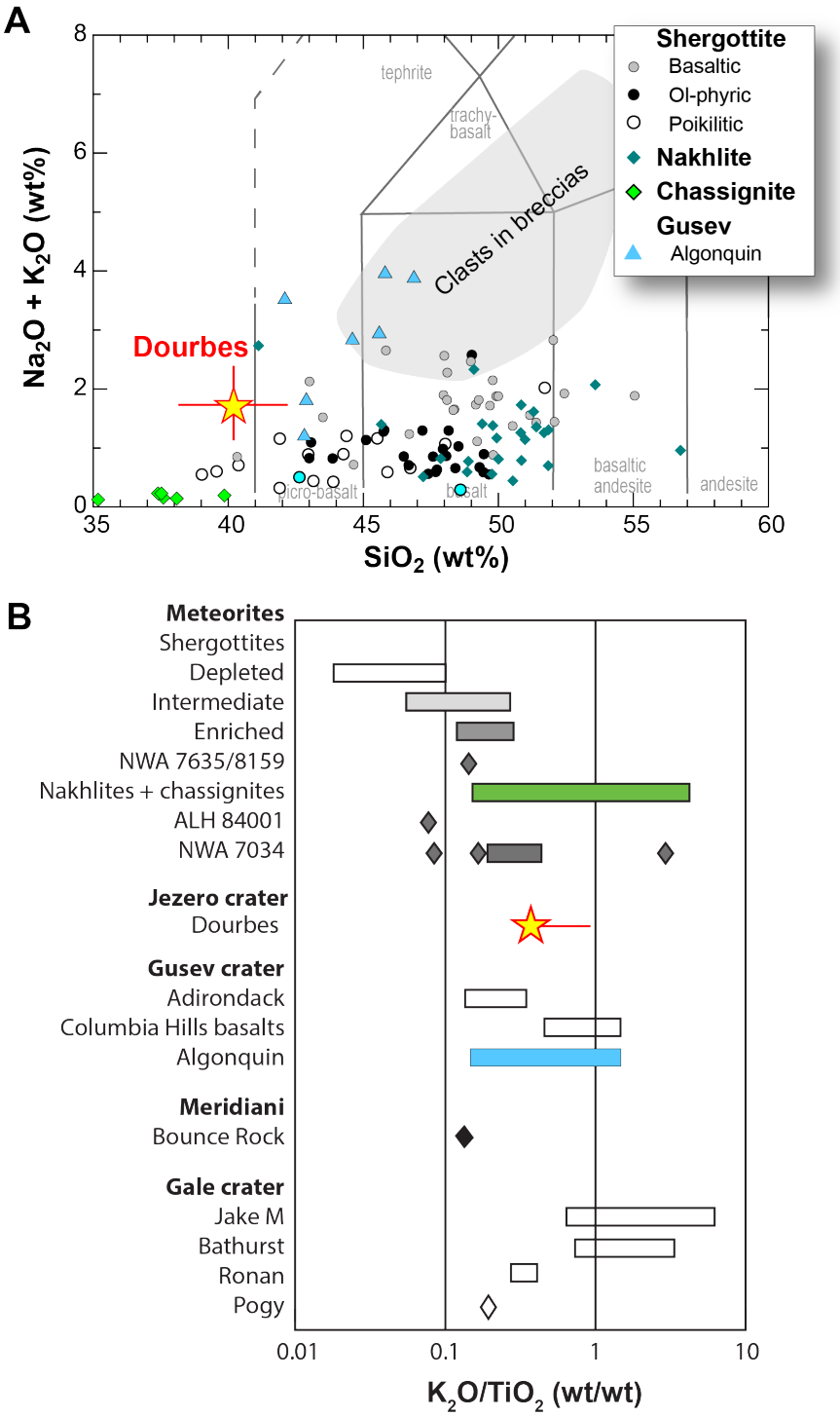

Fig. 4. Bulk chemistry of Dourbes compared to meteorites and igneous rocks elsewhere on Mars. (A) Total alkali oxides - SiO_2 diagram. Fields defined by vertical gray lines show the classification of volcanic rocks by (*37*). The gray field shows igneous clasts in breccia meteorite NWA 7034 (*38*). Dourbes contains less SiO_2 and higher alkali metal oxides than other Martian igneous rocks. (B) Weight percentage ratios of K_2O/TiO_2 of Dourbes and other Martian igneous rocks. Horizontal bars show the range of values from different samples labelled on the left. Filled diamonds show individual samples. Dourbes is most similar to K-enriched meteorites, such as

chassignite and nakhlite, and the Algonquin rock in Gusev crater. Dourbes data are plotted as star symbols with estimated 1σ uncertainty. Dourbes data are listed in Table S5 and data sources for meteorites and rover data are listed in Table S7.

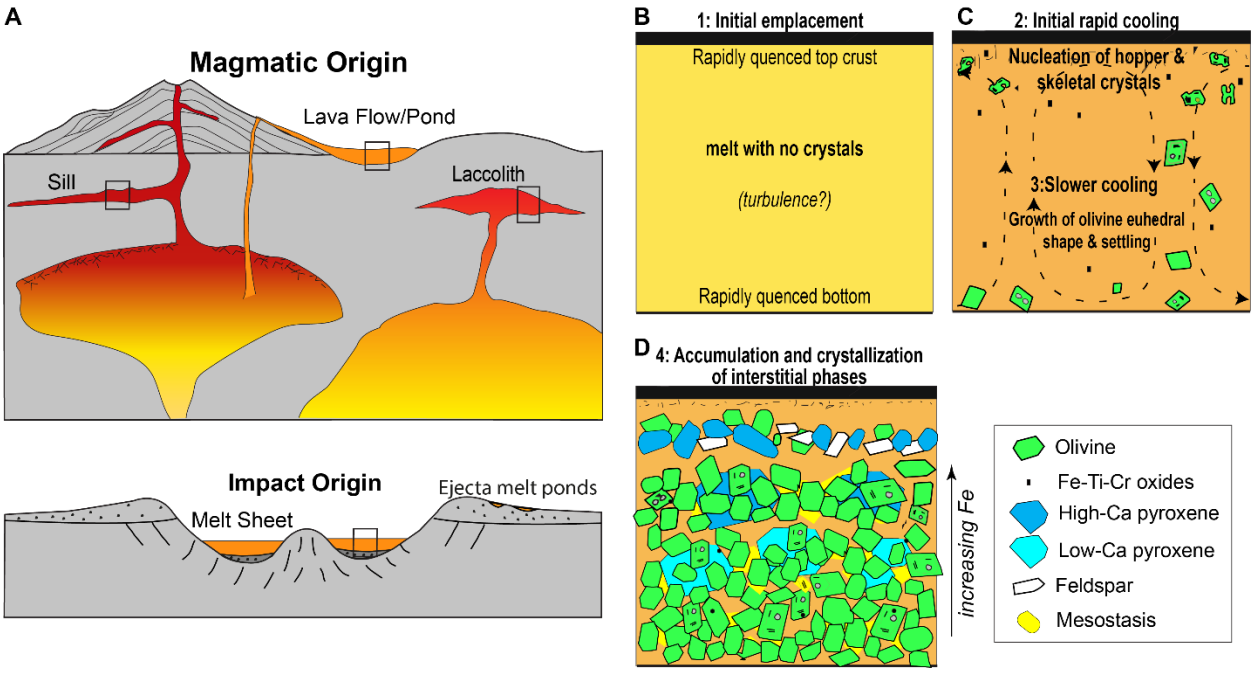

Fig. 5. Schematic diagram of potential emplacement models. (A) Potential emplacement models for the Bastide member, which hosts the Brac and Batide outcrops. Color hue schematically indicates the temperature of the melt, darker means cooler. Possible scenarios are an extrusive lava flow/pond, an intrusive sill or a small laccolith, or an impact melt sheet or ejecta melt pond. All models provide the range of cooling rates as we infer for the Brac outcrop. Panels B-D show the petrology of our model (not to scale). (B) Initial emplacement of melt without any crystals, forming a rapidly quenched top crust and bottom. (C) Rapid cooling after emplacement causes nucleation and growth of hopper or skeletal olivine grains near the top surface. Convection of olivine into the (more slowly cooling) interior promotes olivine growth. Once each crystal reaches a critical size, it sinks to the bottom. (D) Continued cooling, crystallization and sinking concentrates olivine at the base. Further crystallization of low-Ca pyroxene, high-Ca pyroxene and other minerals (indicated in the legend) form stratified layers, with increasing Fe contents higher in the melt body.

Science
AAAS

Supplementary Materials for

An olivine cumulate outcrop on the floor of Jezero crater, Mars

Y. Liu*, M.M. Tice, M.E. Schmidt, A.H. Treiman, T.V. Kizovski, J.A. Hurowitz, A.C. Allwood, J. Henneke, D.A.K. Pedersen, S.J. VanBommel, M.W.M. Jones, A.L. Knight, B.J. Orenstein, B.C. Clark, W.T. Elam, C.M. Heirwegh, T. Barber, L.W. Beegle, K. Benzerara, S. Bernard, O. Beyssac, T. Bosak, A.J. Brown, E.L. Cardarelli, D.C. Catling, J.R. Christian, E.A. Cloutis, B.A. Cohen, S. Davidoff, A.G. Fairén, K.A. Farley, D.O. Flannery, A. Galvin, J.P. Grotzinger, S. Gupta, J. Hall, C.D.K. Herd, K. Hickman-Lewis, R.P. Hodyss, B.H.N. Horgan, J.R. Johnson, J.L. Jørgensen, L.C. Kah, J.N. Maki, L. Mandon, N. Mangold, F.M. McCubbin, S.M. McLennan, K. Moore, M. Nachon, P. Nemere, L.D. Nothdurft, J.I. Núñez, L. O'Neil, C.M. Quantin-Nataf, V. Sautter, D.L Shuster, K.L. Siebach, J.I. Simon, K.P. Sinclair, K.M. Stack, A. Steele, J.D. Tarnas, N.J. Tosca, K. Uckert, A. Udry, L.A. Wade, B.P. Weiss, R.C. Wiens, K.H. Williford, M. Zorzano

*Correspondence address:
Jet Propulsion Laboratory, California Institute of Technology, Pasadena, CA 91109, USA.
yang.liu@jpl.nasa.gov

This PDF file includes:

Other Supplementary Materials for this manuscript:

Movie S1

Materials and Methods

The PIXL instrument

PIXL *(15)* has three major subsystems. First, an x-ray fluorescence (XRF) subsystem with a 28 kV high-voltage power supply focuses a polychromatic x-ray beam on target surfaces and detects fluorescent and diffracted x-rays via two silicon drift detectors (referred to as detector A and B). The polychromatic x-ray is generated in an x-ray tube, manufactured by Moxtek, Inc., by focusing the electron beam from a tungsten-filament operated at 1 V and 20 μA, onto a rhodium target mounted on the tip of a tungsten alloy anode maintained at + 28 kV. A modeled energy spectrum of the x-ray tube with optics is shown in Fig. S9. The x-ray beam size on the target surface is x-ray energy dependent. It is the smallest with a diameter of 120 μm when the distance between the rock surface and instrument face is 25.5 mm, the optimal standoff distance. Second, an optical fiducial subsystem (OFS) consists of a Micro-Context Camera (MCC) paired with a multispectral floodlight illuminator (FLI) and two structured light illuminators (SLIs). The OFS collects context images of targets at a nominal resolution of 50 μm per pixel at the optimal standoff distance, covering a 39 mm × 31 mm area, larger than the XRF analysis. The FLI provides multispectral illumination with a set of near-infrared (NIR, 735 nm), green (G, 530 nm), blue (B, 450 nm), and ultraviolet (UV, 385 nm) Light Emitting Diodes (LEDs) that enables analysis based on single channel grayscale images, false color composed images, or relative reflectance ratios. Third, a 6-strut hexapod motion control system is directed to steer PIXL's x-ray beam across targets, while autonomously adjusting for topography to maintain focus, and for thermal deflection of the rover arm to maintain the desired scan pattern based on the distances measured by OFS using a NIR structured light illuminator laser grid.

PIXL observations of outcrops in the Séítah formation, Jezero

Two different outcrops, informally named as Bastide and Brac, in the Bastide member of the Séítah formation were prepared using an abrasion drill bit (*5*, *39*). PIXL collected reflected light images of the abraded patch (informally named Garde) on the Bastide outcrop at a 4.5 cm standoff distance on Sol 208, and of the Dourbes patch on the Brac outcrop at a 4.1 cm standoff distances on Sol 255. At these standoff distances, the field of view of the MCC is ~46 mm × ~39 mm with a resolution of ~65 μm/pixel.

PIXL performed two XRF map scans on Dourbes at the optimal standoff distance of 25.5 mm (Fig. 2A). Scan 1 on Sol 257 covers an area of 4.0 × 12.5 mm and scan 2 on Sol 269 covers an area of 5.0 × 7.0 mm (Figs. S3-S4). With a step size of 125 μm between points, the two maps contain 3333 and 2337 points, respectively. At each point, the x-ray system dwelled for 10 s, acquiring an energy-dispersive XRF spectrum in each of the two detectors. During the scan, the PIXL flight software used the OFS to track the local rock relief and maintain focus of the x-ray beam. It also compensated for the instrument's positional drift induced by thermal expansion and contraction of rover hardware, including the robotic arm that PIXL is mounted to. For PIXL XRF points between each positional check point, the beam locations were interpolated.

Processing MCC images

We performed radiometric calibration of the FLI using a flight-spare OFS at the Technical University of Denmark and using the assembled PIXL flight sensor head at Jet Propulsion Laboratory. The processing methodology was developed using radiometric calibration on a white flat plate that offered spectrally uniform response with diffuse reflectance properties. Raw

images were flat-field corrected and spectrally equalized by compensating for different radiant power emitted by the FLI LEDs, the spectrally dependent sensitivity of the MCC, the shutter time (different for each color) and dark-level (which is thermally dependent). MCC and FLI were calibrated together. The intensity of the band-to-band uncertainty is ~1 %. At high standoffs and with uneven topography on the target, we expect a relative uncertainty of 1-3 %.

Data products were constructed from these corrected raw images, including a composite RGB image and color ratio images (Figs. 1 and S2). The radiometric correction requires the 3D position information determined from the MCC-SLI measurements (*15*, *40*). The unabraded area around the Dourbes patch is outside the coverage of the SLIs. As such, the radiometric correction in the outer rim of the MCC images is over-compensated due to the lack of topographic knowledge. The MCC images were maintained in their raw format, which has a slight trapezoidal surface coverage, due to MCC observing the surface at an ~18° tilted viewpoint relative to the surface normal. This causes a small foreshortening effect along the vertical axis of the images, which is negligible in the central portion of the image.

Quantification of PIXL XRF data by PIQUANT

Elemental quantifications are conducted using a physics-based fundamental parameters approach integrated into the PIQUANT (*15*, *41*) software package. PIQUANT analysis considers the effects of measurement geometry, instrument construction and x-ray transmission through the optic and environmental conditions. PIQUANT modeling of the acquired spectra using a combination of Gaussian line shapes fitted to the observed peaks, informed by theoretical positions of elemental K-shell or L-shell x-ray peaks, as well as tails and shelves resulting from incomplete charge collection within the detector. Bremsstrahlung background is subtracted using a combination of physics calculations and empirical modeling. In-house PIQUANT software derives composition through an iterative fundamental physics calculation process. Convergence on final elemental compositions is realized when the final two software iterations differ by no more than 0.1 % relative for any element. All elements in this study are expressed as oxides except for Cl and Br, and all Fe is assumed to be in the Fe^{2+} state.

Derived compositional uncertainties are based on the calibration performed pre-flight on PIXL using a set of 30 homogenous (or nearly homogenous) geological reference materials (GRMs) or pure element or simple compound substrates (*41*). XRF spectra were collected with an integration time of 2 hours for each GRM and 5 minutes for each pure material. The compositional results for each element in each target as determined by PIQUANT were assessed for discrepancy relative to certificate or stoichiometrically predicted values. Calculations of the root mean square error (RMSE) of the elemental discrepancies were performed and assessed at concentration thresholds of 0, 0.05, 0.5, 5 and 100 wt%. In this manner, the RMSE's cover the full 0 – 100 wt% range at the 1-sigma level and can take on values that are dependent on elemental concentrations in the sample. These are the uncertainties reported by PIQUANT. Spectra with shorter integration times are expected to have larger uncertainties owing to increased statistical noise. Statistical noise can be reduced through forming composite spectra by summing spectra from scanned areas of a similar composition. This improves signal-to-noise and thus lowers uncertainties in spectral assessments that are propagated forward onto compositional results.

Because natural rock materials contain multiple mineral phases, this introduces an additional effect of x-ray diffraction scattering that produces spurious peak artifacts in spectra, often around characteristic Na, Cl, Ti, V, Mn, Fe, and Ni K-shell x-ray peaks. As the detector

response to diffraction peaks is not typically mirrored between both detectors, the effect of diffraction peaks on the quantification was recognized by comparing spectra (and spectral analyses) from detectors individually. In the reported data (Tables S2-S5), we did not correct the diffraction peak effects.

Calculating bulk and mineral compositions

We quantified the bulk chemistry of Dourbes from the sum spectra of all points of both detectors, detector A, and detector B, respectively (Table S5). The bulk sum spectra for detector A and B are shown in Fig. S10. In addition, the texturally-correlated compositional data allow us to separate different minerals, specifically primary minerals from secondary materials. We define the unaltered primary regions (hereafter referred to as pristine) in scans to be points with SO_3 <1 wt% and Cl < 1 wt% and with diffraction peaks. The bulk chemistry of the pristine rock is calculated using the sum spectrum of all points fulfilling the above criteria. Given the presence of diffraction peaks near Na, Cl, Ti, V, Mn, Fe, and Ni K-shell x-ray peaks, our reported uncertainties of bulk rock and bulk pristine rock (Table S5) include uncertainties estimated from the above quantification approach and additional values (typically 5-10 % relative) where spectral analysis indicated the presence of diffraction peaks.

For the coarse olivine and augite grains in Dourbes, we used the average chemistry of interior points to avoid compositional mixing effects with adjacent phases. We corrected for the presence of salts by removing Ca:S and Na:Cl at a 1:1 molar ratio . This correction is negligible for both phases, as the original data contain < 0.3 wt% SO_3 and < 0.4 wt% Cl (Tables S2-S3). For olivine, we further renormalized the corrected values to be K-Al free, which is also a small correction as the original Al_2O_3 concentrations are <0.23 wt%.

The grain sizes of feldspar, phosphate, and Fe-Ti-Cr oxides are no larger than the x-ray beam. We did not derive the chemistry of these minerals as they are compromised by mixing of neighboring mineral phases. Based on elemental association, we can identify the presence of Na-feldspar, K-feldspar, different Fe-Ti-Cr oxides, and merrillite.

Mineral domain clustering analysis using back-reflected diffraction data

Because PIXL features two x-ray detectors (detector A and B) on either side of the x-ray source, anisotropic crystal diffraction peaks can be detected and distinguished from isotropic fluorescence peaks (*42*). Although diffraction peaks often limit quantification (as discussed above), their presence can be advantageous in determining crystal properties of the minerals being analyzed (*42*). In the most basic analysis, the presence of diffraction peaks means that a crystalline material is present, while their absence implies either amorphous materials or the presence of crystal domains substantially smaller than the x-ray beam diameter. As the two x-ray detectors on PIXL are equally spaced from the x-ray source, powder samples will diffract equally in both detectors and therefore not be as easily detected and distinguished as crystalline diffraction. However, due to the short integration times per point and high diffraction angle, PIXL is insensitive to diffraction from powdered materials.

The energy of a diffraction peak or set of diffraction peaks recorded in a single detector is directly related to the mineral properties and grain orientation of the target material. If the crystal domain size is larger than the beam size, then a set of diffraction peaks will persist at the same energies and relative intensities in neighboring measurement points. In a PIXL measurement, we can therefore determine whether a set of adjacent measurement points with the same elemental compositions and diffraction peaks relates to a single crystal domain.

For the pyroxene regions in scan 1 of Dourbes, we identify two diffraction peaks present in the central embaying pyroxene observed in the first Dourbes scan, one in each detector (Peak 1 and 2 in Fig. S2E). Both peaks are observed over adjacent points in the same contiguous region and among different regions (area 1, 2, 3 in Fig. S2A and regions 1-6 in Fig. S2B). The intensities of these two peaks are correlated (Fig. S2D). We apply similar analyses to several olivine grains (Ol) and confirm that they are single crystals, however unlike the pyroxene (Px), individual olivine grains have different orientations relative to one another (Fig. 2C).

Mineral modal analyses

We use two approaches to estimate the volume percentages of minerals in the abraded patches. Olivine grains appear to have minor alteration interior to their original grain boundaries. This is manifested as lower G/NIR ratios and lower Mg contents (Fig. S1b). We make the simplifying assumption that these altered areas were part of the original primary olivine and count them as olivine.

In the first approach, we count total points in each distinct phase (minerals, mesostasis, and secondary phases) as determined from the chemistry. Because the clear difference of pyroxene and mesostasis from other components, their volume estimates are very accurate. For olivine next to secondary phases, the uncertainty in its original edge leads to an uncertainty of ~3 vol%.

In the second approach, we use MCC G/NIR ratio images. MCC images of abraded patches cover a larger area than XRF scans and thus mineral modal analyses provide information over a larger area of the abraded rocks. Olivine, pyroxene and secondary materials are easily distinguishable in the MCC G/NIR ratio image (Figs. S1B and S1E). Mesostasis is difficult to distinguish from other components. To avoid the over-compensated outer rim of MCC images, we only used the central part of these images (Figs. S1B and S1E). Using the ImageJ (*43*) software package, we counted the total pixels in each color range for each mineral phase, which is defined by setting lower and upper color threshold c. The choice of the threshold introduces uncertainty. Therefore, we conducted two estimates by adjusting the threshold by one intensity value in order to estimate the uncertainty. Because the clear color difference between olivine and pyroxene, this approach provides good estimates of the relative proportions of olivine and augite in both Garde and Dourbes. The similar results between two approaches provide a verification of the modal percentages (Table S1).

PIXL Data Visualization

We used PIXLISE *(106-109)*, a data visualization software package developed specifically for the interpretation of PIXL data, for our analysis.

Supplementary Text

Texture of Garde and Dourbes from PIXL MCC images

Informed by the XRF elemental analyses on Dourbes, beige grains are olivines, greenish gray areas are augites, and reddish brown areas are secondary regions in the reconstructed color (NIR-G-B) MCC image (Fig. S1A). The grain shape and boundaries are visible in color ratio images of the abraded patches, especially in the G/NIR ratio image (Fig. S1), with both Garde and Dourbes displaying similar textures. Modal abundances of olivine and augite analyzed with the MCC images of Garde are similar to those in Dourbes (Table S1). These results suggest the XRF observation of the Brac outcrop can be extended to the Bastide outcrop in the Séítah formation.

Petrography and chemistry of Dourbes from PIXL

Figures 1 and S1- S4 show textures of areas imaged and scanned by PIXL. Movie S1 shows the co-located PIXL XRF maps and MCC images with images from other cameras on the rover (image sources in Table S7). Crystallinity of olivine, pyroxene, and mesostasis are confirmed by the presence of diffraction peaks (Fig. S2). Persistent presence of diffraction peaks of same energies in different augite regions imply all regions have a single orientation, and are likely part of a single crystal domain (Fig. S2). Olivine grains were altered to different degrees. However, the overall shape of olivine grains including alteration is euhedral. Many olivine grains touch corners or sides forming the framework of the accumulated olivine grains. The mesostasis shows significant variations in its chemical composition reflecting variations in the proportion of plagioclase, phosphate, and oxide minerals (Table S4, Figs. S3 and S4).

Table S1 shows the estimate of mineral abundances in the studied areas. As feldspar is part of the mesostasis, its abundances are less than that of mesostasis (i.e., < 1 vol%). Based on the olivine percentage and assuming pyroxene crystallized from the interstitial region of olivine, the space between olivine grains suggests that the porosity in the cumulated olivine framework is 35 ± 5 vol% of the studied area. Several olivine grains contain possible melt inclusions ranging from 100 to 600 μm long (Figs. 1, S3, and S4).

Tables S2-S4 list compositions of four different olivine grains, two pyroxene grains, and six different mesostasis regions. Only the interior points and unaltered regions were included for these analyses. We calculated olivine and pyroxene compositions using both the original data and those after correcting for salt contamination (i.e., remove Ca and Na, assuming 1:1 molar ratios with S and Cl, respectively, Tables S2-S3). Given their physical proximity, apparent intergrowth and uniform compositions, olivine and augite likely equilibrated during the cooling of their parent melt body. Using the Fe-Mg exchange geothermometer between olivine and augite (*44*), we obtained an equilibration temperature of 1085^{+27}_{-25} °C (Table S6).

Two scan areas show large differences in mineralogy, in that second scan contains more mesostasis and fewer pyroxene grains. The second scan area only contains Fe-Cr-Ti oxide grains with the lowest Cr/Ti ratios (Fig. S6). Calcium-phosphate grains in both scan areas are similar and only present in the mesostasis. The trend of all XRF points in a ternary diagram (Fig. S7) indicates the Ca/P ratios of the phosphate endmember is most consistent with that of merrillite, which is common in shergottite Martian meteorites (*45*) (Fig. S7).

The bulk chemistry of Dourbes determined from both detectors or individual detectors is consistent, indicating diffraction interference to Na, Cl, Ti, V, Mn, and Ni *K*α is small (Table S5). The difference in Mn reflects the effect of the diffraction peak near the Mn *K*α x-ray peak.

The Na, K, S, and Cl abundances of the pristine regions are lower than those of uncorrected original sum (Table S5), indicating that secondary materials also contain higher Na and K contents.

Comparison to Martian igneous rocks

Many igneous Martian meteorites are cumulate rocks, including the orthopyroxenite Allan Hills 84001; the chassignite meteorites (which contain dunite); the nakhlite meteorites (which are clinopyroxene-rich); and two groups of shergottite meteorites (poikilitic and gabbroic) (*26*, *46*, *47*).

Poikilitic shergottites consist of variable amounts of olivine, pyroxene, and plagioclase with compositions ranging from mafic to ultramafic (*21*) (Fig. 3C). Olivine grains in these shergottites typically display distinct compositional variations between those inside the poikilitic pyroxenes and those in surrounding feldspar-rich areas (*21*, *48*, *49*). Olivine grains enclosed in the poikilitic regions have varying compositions (Fig. 3A), are rounded and typically < 1.8 mm, while the olivine grains in the surrounding feldspar-rich areas show little compositional variation (*21*, *48*, *49*). The pyroxene grains are also typically zoned from Ca-poor interior to Ca-rich rims (*21*, *48*, *49*). The grain size and compositional variations of olivine and pyroxene in poikilitic shergottites are distinct from Dourbes (Fig. 3A).

Only three chassignites have been identified: Northwest Africa (NWA) 8694, Chassigny, and NWA 2737, compared to ~300 other Martian meteorites (*50*). The chassignites consist mostly of euhedral to subhedral olivines, which are chemically homogeneous (*28*). The average lengths of olivine grains are 0.48 ± 0.30 mm for Chassigny (Fig. 2B) and 0.64 ± 0.48 mm for NWA 2737 (*28*), whereas those in NWA 8694 are <1 mm. The olivine composition varies among three chassignites with Fo contents of 53, 68, and 79 for NWA 8694, Chassigny, and NWA 2737, respectively (*28, 51*). Chassignite olivine grains also contain magmatic inclusions — aliquots of original magma trapped among irregularities on the crystal surfaces as they grew (white circle in Fig. 2B). Some olivine grains in chassignites are enclosed poikilitically by anhedral pyroxene (Fig. 2B). The remaining <10 % of the rocks is mesostasis material, containing Fe-Ti-Cr oxides and small grains of plagioclase with minor minerals (e.g., Fe-Ti oxides, alkali feldspar, apatite).

Despite having a similar texture, Dourbes differs from chassignites in bulk chemistry and mineralogy. Dourbes only contains high-Ca pyroxene (augite) whereas chassignites contain both high-Ca and low-Ca pyroxenes (Fig. 3A). These mineralogical differences reflect differences in melt compositions. The bulk chemistry of Dourbes shows that it contains more alkali metals than all Martian igneous meteorites (Fig. 4A) and within the range of poikilitic shergottites in the Ca/Si-Mg/Si ternary diagram (Fig. S8). An additional difference between Dourbes and the chassignites is in the Ca-phosphate mineralogy. The chassignites contain apatite with no merrillite, while the Ca-phosphates in Dourbes have Ca/P ratios more similar to merrillite (Fig. S7). This difference in Ca-phosphate mineralogy could indicate differences in magmatic volatiles in their respective parental magmas, as expected if volatile abundances in Mars' interior are heterogeneous, both spatially and temporally. Alternatively, the chassignites could have had eruption histories that allowed for different retention of volatiles prior to phosphate saturation in the inter-cumulus melt. Together, the mineralogical and bulk chemical composition of Dourbes show it is distinct from Martian meteorites (Figs. 3 and 4A).

Previous Mars rovers Spirit, Opportunity, and Curiosity have observed diverse igneous rocks at their landing sites that are complementary to Martian meteorites. Those lithologies are

predominantly basaltic, including tholeiitic, alkali-rich, and evolved alkaline compositions (*34, 52–54*). Many of those rocks are loose rocks not associated with outcrops, except for some outcrops investigated at Gusev Crater by the Spirit rover. At Gusev crater, an ultramafic lithology was encountered by the Spirit rover at olivine-rich outcrops in the Columbia Hills, called the Algonquin class, and includes the carbonate-bearing Comanche outcrop (*55*, *56*). The granular to massive textures of these rocks were interpreted as indicating a volcaniclastic origin (*57*), while a correlation between Mg, Ni, and Cr content with distance driven by the rover led to the suggestion that these variations may reflect olivine accumulation in a mafic-ultramafic magma body (*58*). The ultramafic mineralogy and composition of Dourbes are similar to the olivine-rich Algonquin class of Gusev crater (*57*, *58*), but Dourbes contains less SiO_2 and alkalis, suggesting more mafic minerals than the Algonquin rocks (Fig. 4A).

Parent melts

The parent melt of cumulate rocks is difficult to constrain. Methods for doing so can be grouped into the following approaches: First, the parent melt can be inferred from olivine-hosted melt inclusions (*26*, *59*, *60*), which are small parcels of melt trapped by the olivine. As olivine is typically the first mineral to form from the melt, the melt inclusion is closest to the parent melt composition. However, after the melt is trapped by olivine, its chemistry is modified due to additional olivine crystallization onto the wall of the inclusion (post-entrapment crystallization) and diffusive exchange of Fe and Mg with the olivine host - hence outside melt during cooling. Slow cooling with cumulate rocks exacerbates these changes. Therefore, the measured composition of the melt inclusion is often corrected by adding olivine back into the composition until an equilibrium Fe-Mg is reached between inclusion and bulk sample (*61*). Second, the inferred parent melt can be tested through crystallization experiments or thermodynamic modeling in order to reproduce the observed mineralogy (olivine + Fe-Cr oxides, pigeonite or augite, feldspar + Fe-Ti oxides). If different, the inferred melt is corrected by adding additional minerals, often olivine. The above approaches only estimate the melt at the time that the olivine crystallized, because the amount of crystal fractionation leading to the time that olivine formed is unknown (*62*). Previous work estimated the parent melt of Chassigny from the melt inclusions in its olivine gains (*59*). However, crystallization experiments using that melt composition produced pigeonite and then augite with olivine appearing after them (*63*, *64*), which is opposite to the inferred crystallization sequence for Chassigny. In addition, the olivine that crystallized from the experimental charges is more Fe rich (Fo < 40) than those in the chassignites and Dourbes (Fo > 53).

The parent melt of NWA 2373 has previously been inferred from its olivine-hosted melt inclusions (*60*). Thermodynamic calculation of this parent melt showed that the calculated olivine composition is similar to Chassigny and NWA 2737 (*60*). However, the calculated crystallization trend suggests that augite crystallizes before the crystallization of Fe-rich olivines (Fo_{50-55}), which is also opposite to the observed crystallization sequence.

For the ferroan-chassignite NWA 8694, a melt composition has been calculated (*51*) by adding Nakhla core olivine composition (*26*) to that of the olivine-hosted melt inclusions from a primitive nakhlite (*66*). The crystallization sequence was then calculated (*51*) using this inferred parent melt for NWA 8694. Their results show that Fo_{50-55} olivine crystalizes first and then followed by co-crystallization with augite until 80 wt% crystallization, which matches the crystallization sequence we infer for Dourbes. This parent melt contains Mg# of 27, indicating

the source is Fe-rich or the parent melt is the evolved residual melt after a high degree of crystal fractionation of a more primitive (Mg-rich) melt.

By comparing with those analyses of chassignites, we place constraints on the parent melt of Dourbes from olivine chemistry. The Fe/Mg ratios of Dourbes olivine grains suggest that the melt was Fe rich with a Mg# of 27-30, similar to the inferred NWA 8694 parent melt (*51*). Thermodynamics calculation (*51*) of the proposed parent melt for NWA 8694 generated Fo_{50-54} olivine at 1144-1188 °C and then augite at 1085 °C, which is similar to the inferred equilibrium temperature between Dourbes augite and olivine, based on the Fe/Mg equilibrium geothermometer (*44*) (Table S6). Because olivine crystallized before augite (as indicated by the poikilitic texture), this temperature is a minimum value at which olivine re-equilibrated with augite. This comparison suggests that the parent melt derived from NWA 8694 can approximate the melt from which Dourbes olivine (and later augite) crystallized. However, the system could have started with a melt of different chemistry and crystallized more Mg-rich olivine and low-Ca pyroxenes before the melt evolved to Dourbes' composition.

Earth analogs

Olivine cumulates are found in different geological settings on Earth, mostly from layered intrusions. Although accumulated olivines have been reported in lava flow or lakes on Earth, their textures differ from the Dourbes wehrlite.

Theo's Flow, a ferropicrite flow of ~120 m thickness in the Neoarchean of Canada's Superior province (*66–68*), hosts rocks analogous to the nakhlite Martian meteorites. Below the nakhlite analogs is a 15-m thick layer of peridotite, where poikilitic augite grains surround and enclose roughly 0.3 mm-sized serpentine aggregates that replace original olivine grains [(*66*), their figure 4]. Similar serpentinized peridotites are found in ultramafic lava flows or lakes in this province (*68–70*). However, modelling of the cooling rate based on closure temperature of single augite grains showed that Theo's Flow was built by multiple magma emplacements (*71*). The olivine grain sizes in Theo's peridotite are smaller than those in Dourbes and chassignites, which is consistent with the emplacement of a 15-m thick flow. The olivine grains in Theo's flow might have formed through rapid growth in the lava or they may have been brought to the surface from a magma storage zone. Olivine cumulates are present at the bottom of individual komatiite flows of <50 m thickness in the Barberton Greenstone Belt, South Africa (*72*). These cumulates contain olivines up to 2 mm and glassy matrix.

Olivine accumulation occurs in mafic lava lakes on Earth, which are usually centered over their vent source and can undergo vigorous convection and differentiation, possibly involving the crystallization and accumulation of olivine, depending on the parental magma composition. An example is the Kilauea Iki picritic eruption of 1959 that generated a ~100 m thick lava lake, which solidified and was repeatedly drilled over ~30 years (*73–75*). Olivine crystallization and gravity-driven accumulation led to the formation of an MgO-rich zone (up to 25 wt%) in the lower portion of the lava lake. Olivine crystals in the Kilauea Iki samples are volumetrically abundant (up to 50 vol%), but rarely touch one another, indicating that rapid cooling by convection in the ~100-m thick lava lake.

Olivine accumulation is also reported at the bottom of komatiite lakes (*76 77*). Komatiites are high Mg ultramafic magma and mostly erupted in the Archean eon on Earth. The ancient komatiite lava-lake in the Vetreny Belt suite on the Baltic shield is an example (*76*). The solidification of the lake was recorded in a thick differentiated lava unit of ~110 m thickness.

From the top to bottom, the lava unit contains scoria, upper chill, layers of spinifex textures, fine-grained basalt, olivine accumulation, and lower chill. The spinifex texture is diagnostic of komatiite flows, indicative of rapid homogenous nucleation of olivine crystals. The olivine accumulation layer is ~20 m thick, containing olivine sitting in a fine-grained matrix [(*76*), their figure 3d]. Olivine grain shapes range from round, polyhedral, elongated grains of <2.5 mm to incomplete (hopper) crystals of <3 mm, which suggests faster cooling than that of Dourbes. For mineral morphology and temperature estimates, a cooling rate of 1.2 to 15 °C/h has been inferred for the layer with hopper and elongated olivine grains (*76*).

These examples show that extrusive melt bodies of ~100 m thickness on Earth do not reproduce the texture in Dourbes: Earth olivine grains are generally smaller and less euhedral, and their groundmasses are glassy. We expect that extrusive bodies cool similarly on Earth and Mars, although the lower gravity and thinner Martian atmosphere cause initially slower cooling immediately after eruption (*78*). Thus, a thicker extrusive body would have been required to provide the slower cooling environment needed to form poikilitic textures and a crystalline matrix. For otherwise identical conditions (same T and melt composition), the settling speed of olivine grains in basaltic magma on Mars is about a factor of 3 lower than that on Earth, which implies the thicker body must have cooled even more slowly for olivine grains to have settled and accumulated. However, in reality, mafic magma on Mars could have different composition and erupt at different temperature from those on Earth. A detailed study is needed to form a close comparison between Earth and Mars.

A single flow of >100 m thickness is not common on Earth. Although large mafic igneous provinces (e.g., flood basalts) on Earth are voluminous, with the total thickness up to a few kilometers, they are typically built by numerous 20-50 m thick flows via inflation (*79–82*). For the same volume-eruption rate and terrain, effusive basaltic volcanism on Mars is expected to generate longer lava flows (*78*). This implies that lava flows would be thinner on Mars than that on Earth for the same erupted mass. On Earth, a thick lava body of ~100 m occurs when topography allows lava to stall, inflate, and pool (such as in a volcanic vent, pre-existing valley or crater) (*81–83*). We expect this is the same on Mars.

An alternative explanation for forming olivine cumulate at the surface is that a thinner melt layer was injected into a warmer environment. For surface environments, an olivine-laden lava from a crystallizing crustal magma chamber injected into a still cooling lava, or an impact melt injected into warmer impact ejecta deposits. For intrusive environments, olivine cumulates of 200-700 m thickness are found in ultramafic units in the komatiitic sequence in the Yilgorn Block of Western Australia (*84*). These units were interpreted as having formed in komatiitic sills (*84*). Alternatively, a crystal-laden melt could have been injected into existing intrusive bodies and then cooled slowly to form cumulates, as suggested for the Palisades sill in the United States (*85*).

On Earth, cumulate rocks are typical of layered mafic intrusions, with large masses of basaltic and ultramafic rocks ranging widely in size (<1 km^2 to >100,000 km^2) and thickness (10s m to ~10 km) (*86*). In these bodies, laterally continuous layers are common, and occur over a range of scales (millimeter and up) and types: by mineral proportions (modal layering), by macroscopic appearances (phase layering), and by mineral compositions independent of their proportions (cryptic layering) (*86, 87*). While gravitational fractionation and accumulation of crystals in magma likely occurs and aids in the development of layering in such bodies, many other processes contribute to their formation. These processes may be dynamic, occurring during filling and crystallization of the magma chamber, or non-dynamic, referring to fluctuations in

intensive parameters that control the liquid line of descent of silicate magmas, such as temperature, pressure, and oxygen fugacity (*87*). Earth layered mafic intrusions occur over a wide range of tectonic environments. The largest intrusions are commonly related to breakups of supercontinents (e.g., Bushveld Complex, South Africa, (*88*)); the smaller layered intrusions have been interpreted as representing the intrusive complements of volcanic systems (e.g., Reinfjiord Complex, Norway; (*89*)). Compared with lava flows and lava lakes, these layered intrusions typically cool much more slowly, as indicated by common presence of overgrowths on cumulate minerals, and the absence of glassy mesostasis material or large melt inclusions, although both are possible in quenched margins of the intrusions (*87*). These features contrast our observations of Dourbes. As such, we do not regard Dourbes formed in large igneous bodies of km thickness.

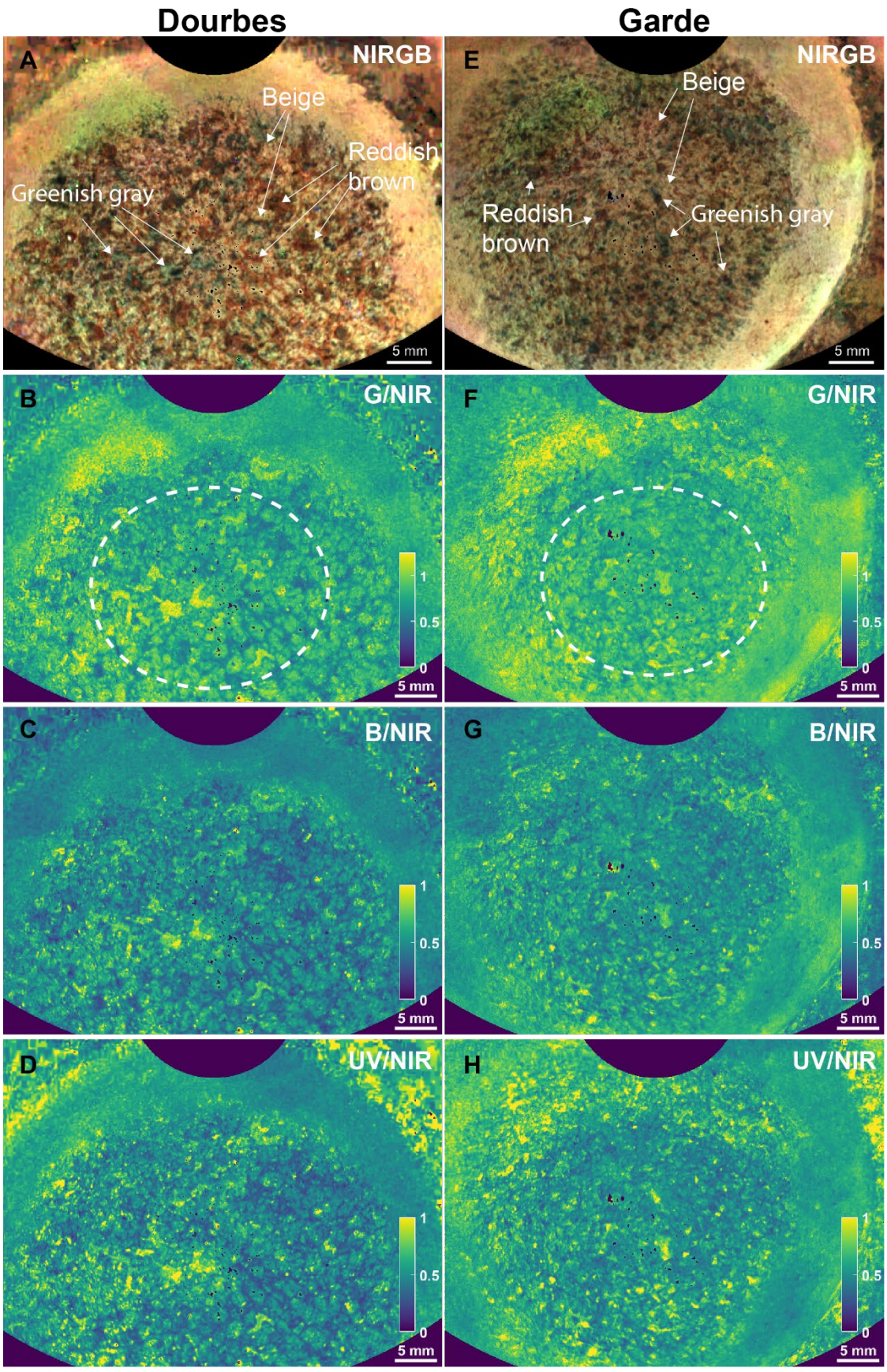
Dourbes
Garde
A
NIRGB
Beige
Reddish brown
Greenish gray
5 mm
E
NIRGB
Beige
Reddish brown
Greenish gray
5 mm
B
G/NIR
1
0.5
0
5 mm
F
G/NIR
1
0.5
0
5 mm
C
B/NIR
1
0.5
0
5 mm
G
B/NIR
1
0.5
0
5 mm
D
UV/NIR
1
0.5
0
5 mm
H
UV/NIR
1
0.5
0
5 mm

Figure S1. MCC images of the Dourbes (A-D) and Garde (E-H) abraded patches, in the Brac and Bastide outcrops of the Bastide member. A) and E) Reconstructed color images using NIR, G, and B images *(102)*. Different minerals display distinct colors. Beige color for olivine, greenish gray for augite, and reddish brown for secondary materials. B) and F) G/NIR ratio images. Ellipses with dashed lines are areas used for analyses of mineral abundances. C) and G) B/NIR ratio images. D) and H) UV/NIR ratio images. The color scales show the ratio values. Overexposed pixels (highly reflective grains) are masked by black color. In B)-D) and E)-F), augite is brighter than olivine, which is brighter than mesostasis and secondary materials.

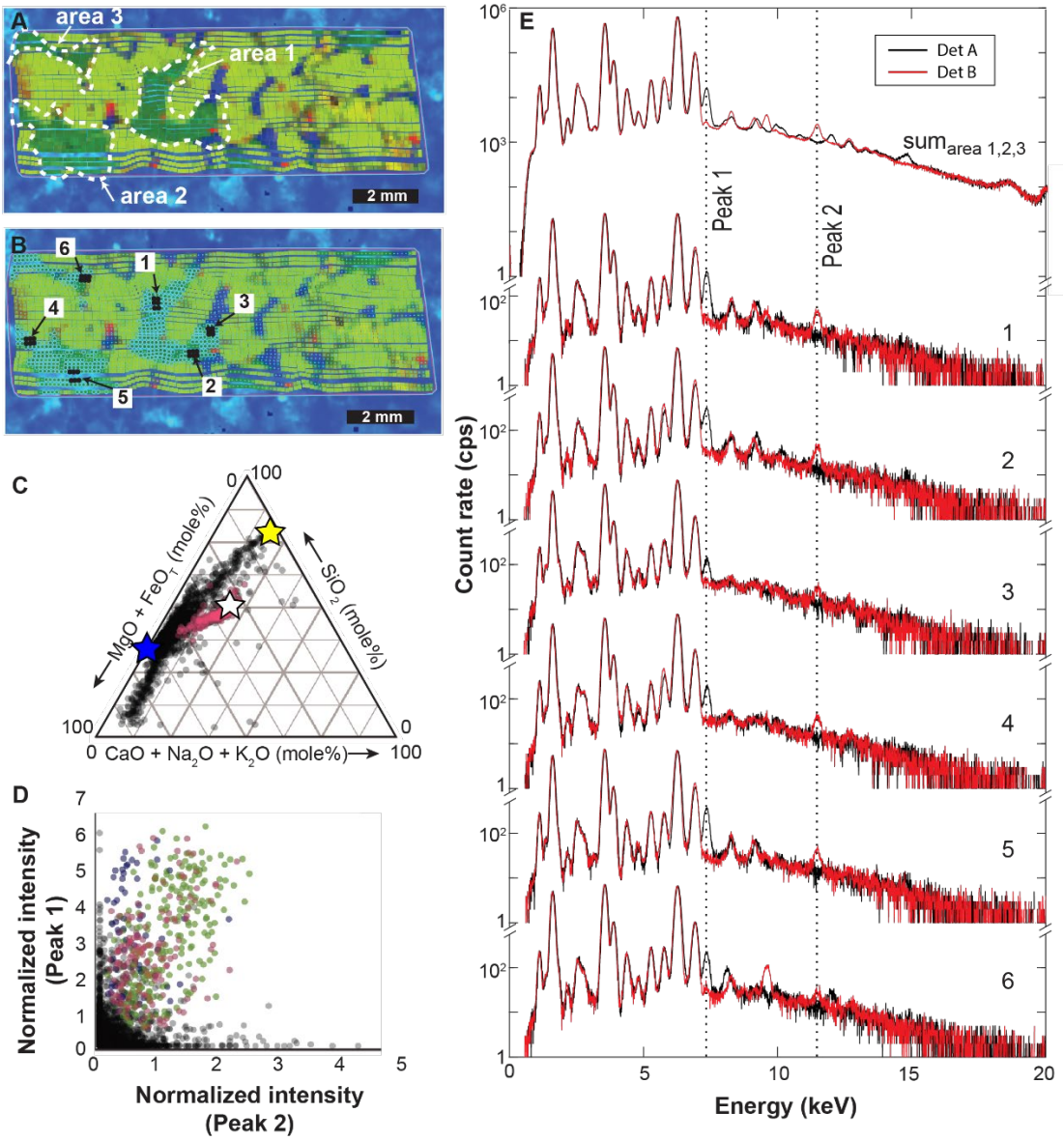

Figure S2. Pyroxene domain clustering analysis. A) FeO-MgO-Al_2O_3 map (color is the same as in Fig. 2D) showing three pyroxene areas (delineated by dotted lines). B) Six individual regions (6 PIXL measurement spots each) of pyroxene showing similar diffraction peak profiles and spectra in panel E. C) Compositional ternary diagram (in molar units) indicating selected regions from panel B (red points) are pyroxene or lie on borders between pyroxene (white star) and olivine (blue star) or mesostasis (yellow star). Black points are all points in the map. D) Integrated counts (background-subtracted and background-normalized) for diffraction peaks 1 and 2 in the areas shown in panel A [green points from area 1, brown points from area 2, and blue points from area 3]. Black points show all points in the map. E) Summed x-ray spectra for three areas marked in panel A and six smaller regions marked in panel B, showing the presence of diffraction peaks across the pyroxene areas. Red and black lines are from the PIXL detectors A and B, respectively. The presence of peaks in two detectors at similar relative intensities over the all the selected areas indicates a common crystal orientation to areas 1, 2, and 3, therefore a single pyroxene crystal domain.

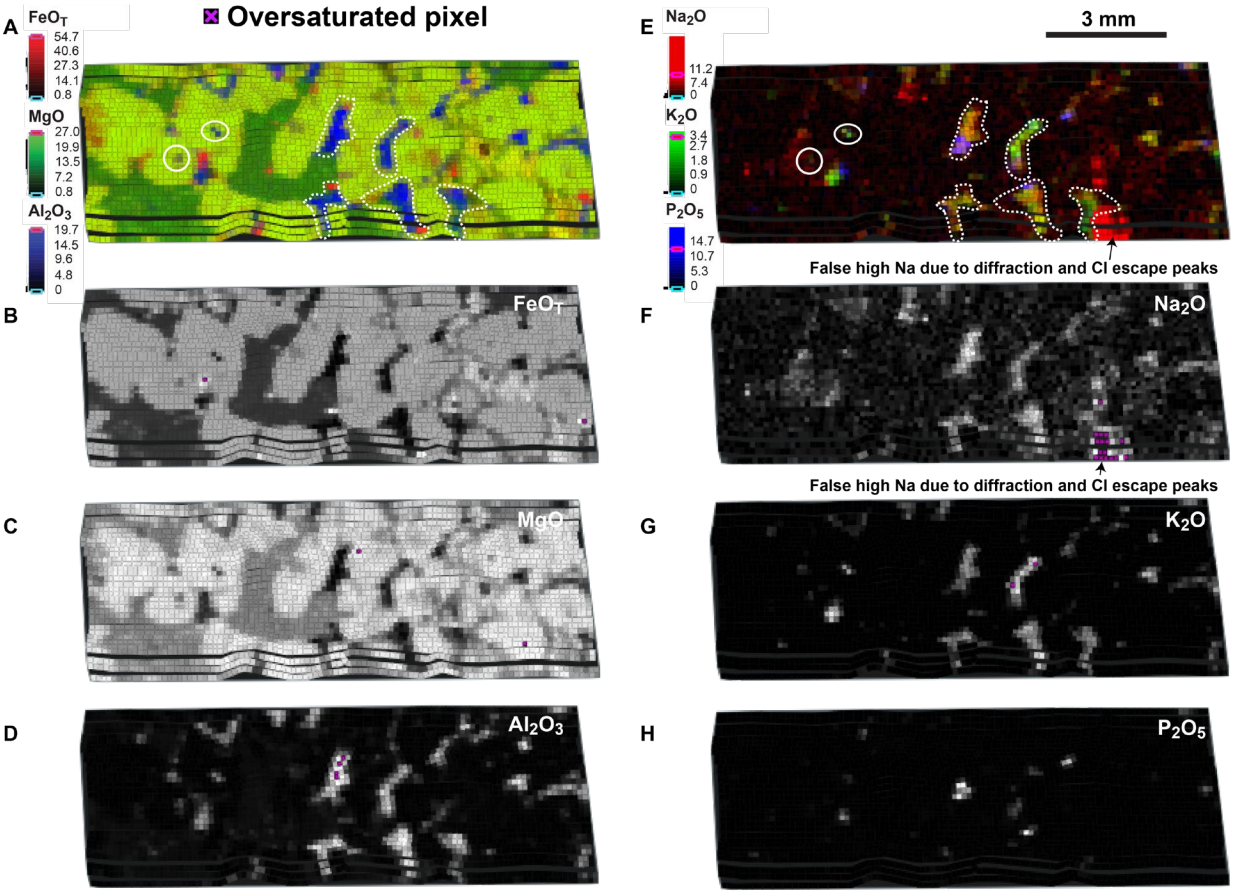

Figure S3. Chemical map derived from x-ray fluorescence of scan 1 in Dourbes (location of scan 1 in Fig. 2A). A) FeO_T (red) – MgO (green) – Al_2O_3 (blue) abundances. B)-D) Grayscale maps of each element in A). E) Na_2O (red) – K_2O (green) – P_2O_5 (blue) abundances. F)-H) Grayscale maps of each element in E). Color scale bars indicate the wt% of the element oxides. The values for the upper limits of grayscale intensities are the same as the color scales in A) and E), respectively. Pixel with a purple × in gray scale images indicates the abundance is above the upper limit set by the color scales in A and E, respectively.

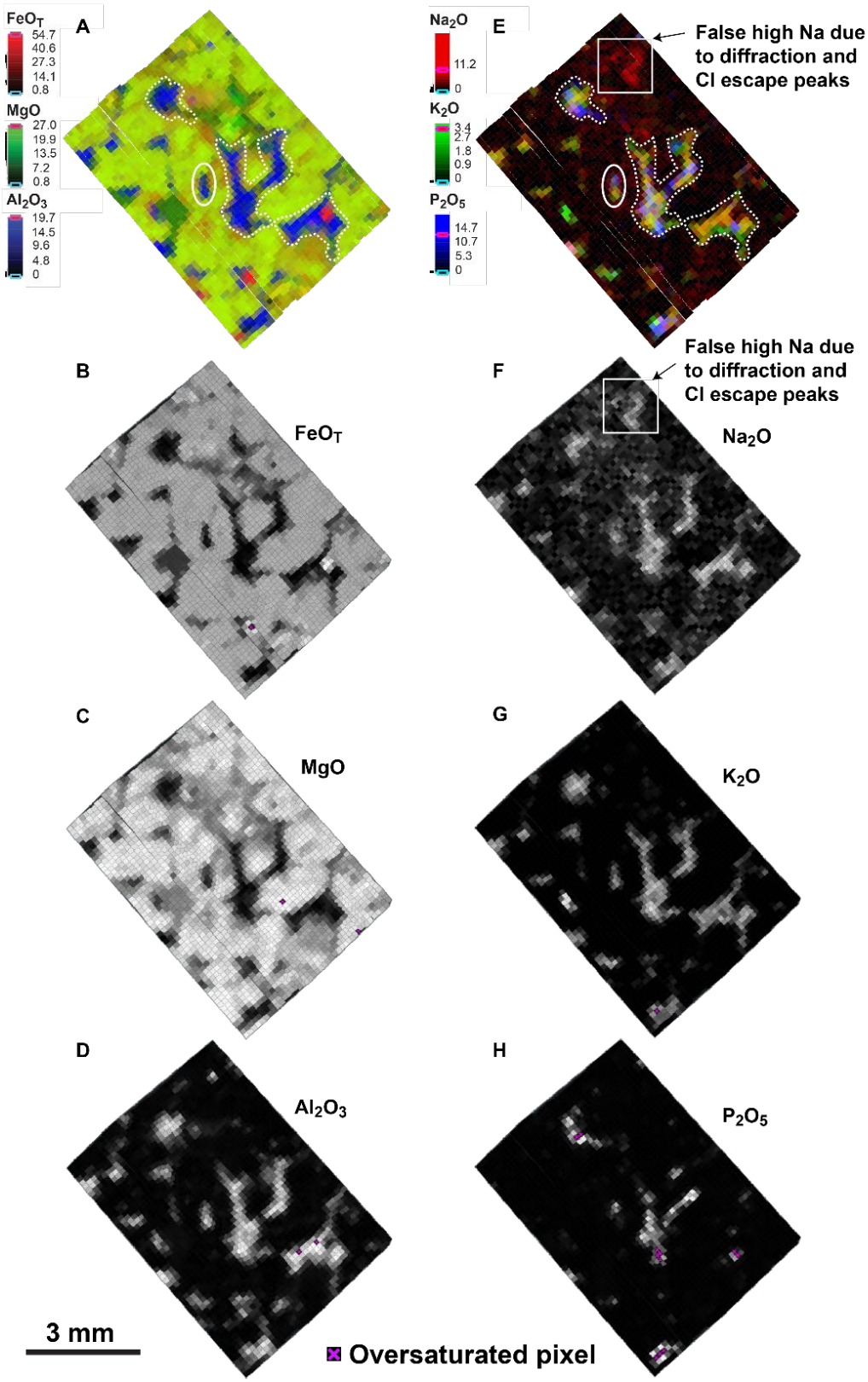

Figure S4. Chemical map derived from x-ray fluorescence of scan 2 in Dourbes (location of scan 2 in Fig. 2A). Color and symbols are same as Fig. S3.

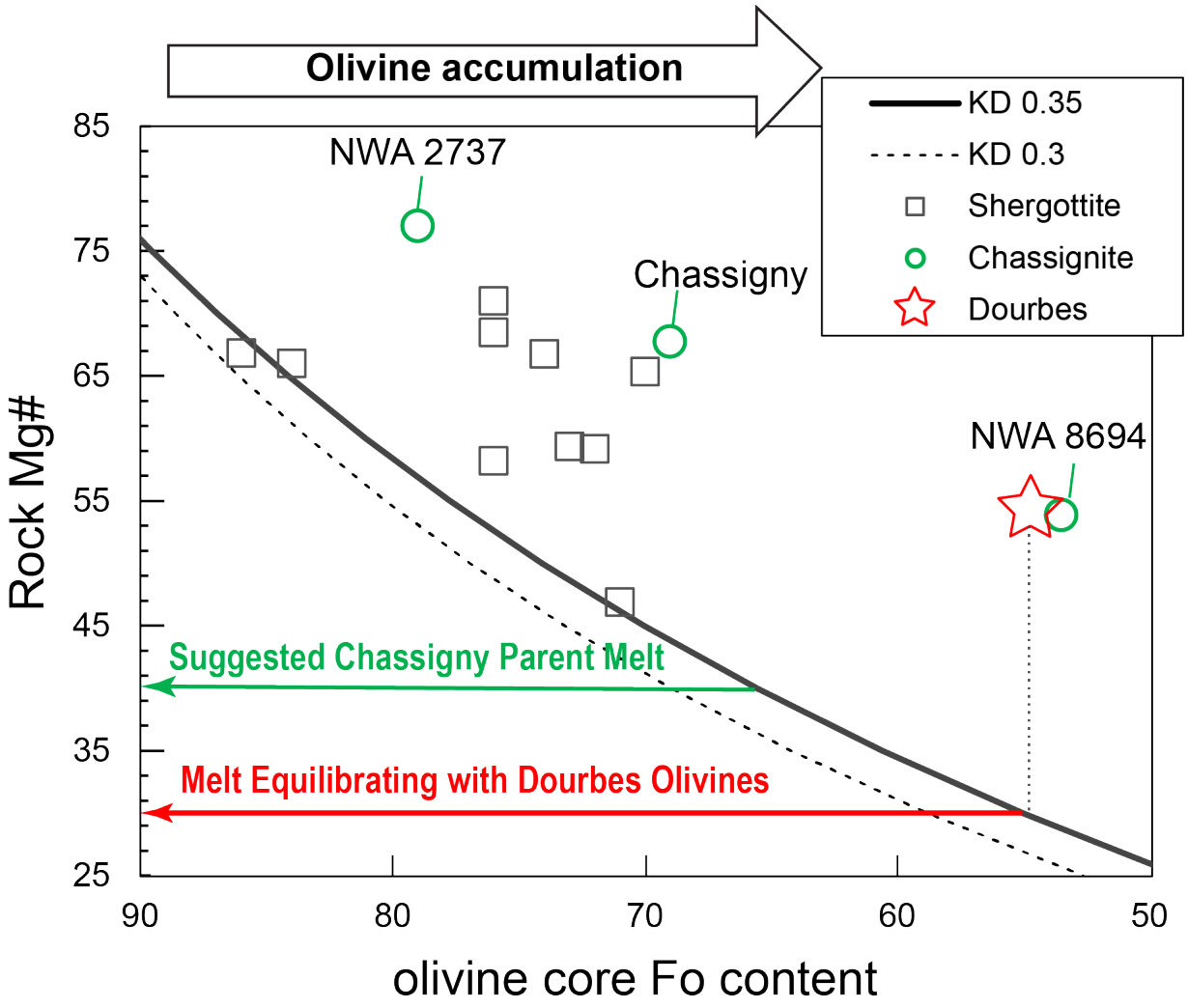

Figure S5. Comparison of olivine core composition in Fo content (mole% forsterite in the olivine) with the bulk rock Mg#. Black curves (solid or dashed) show Mg# of melt that is in equilibrium with olivine. Horizontal lines with arrows indicate the silicate melt Mg# that would have been in Fe-Mg equilibrium with the olivines in Chassigny or Dourbes. Data from (*51, 90*). KD is the equilibrium distribution coefficient of Fe-Mg between olivine and melt. Individual meteorites are labeled.

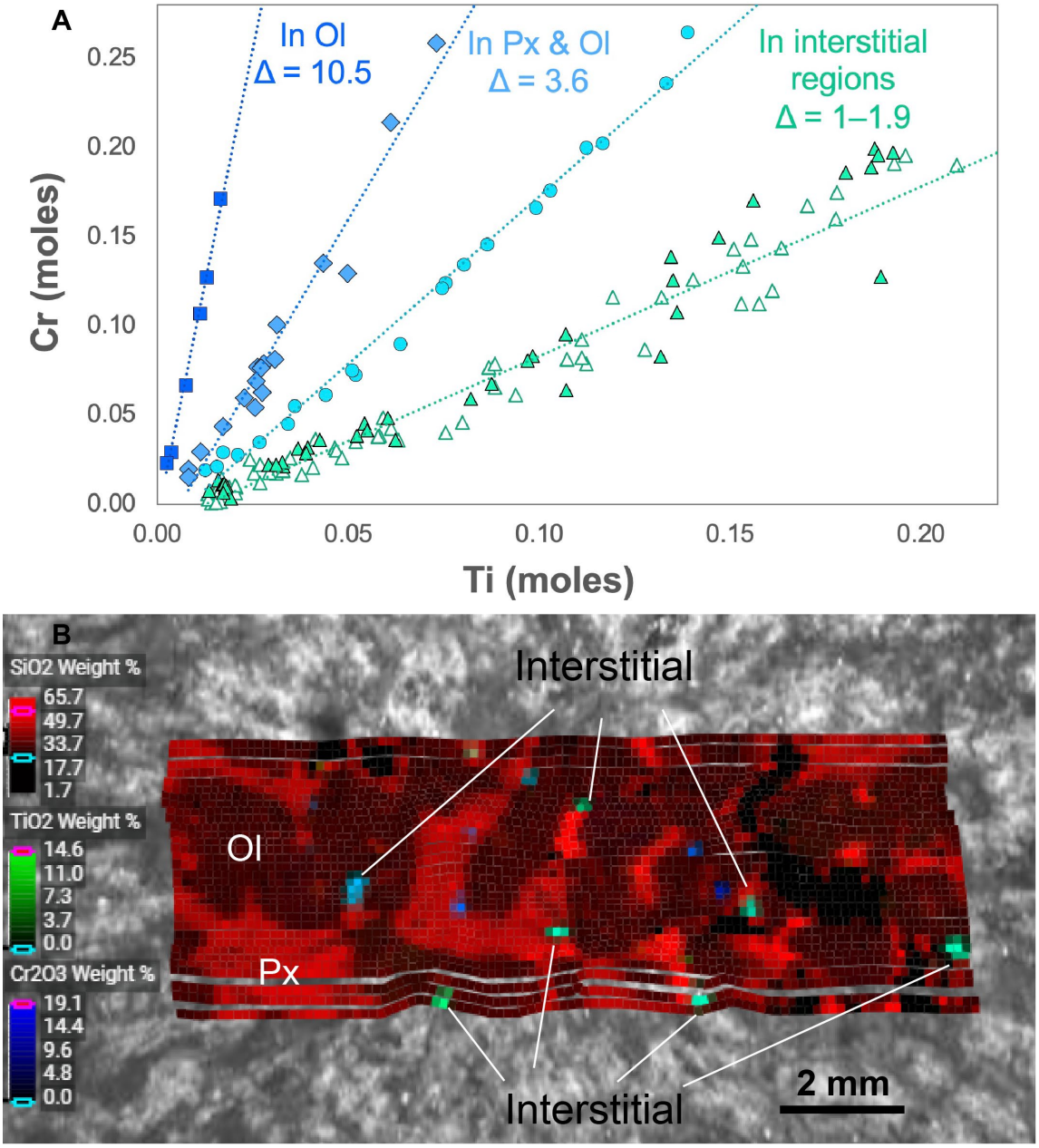

Figure S6. Chemistry of the Fe-Ti-Cr oxides in different petrological contexts. A) Moles of Cr and Ti in Fe-Ti-Cr oxides in different petrological contexts. Δ is the slope of line fitted to the data points. Color of symbols correspond to those in B). Filled data points correspond to scan 1, and unfilled data points correspond to scan 2 (oxides only observed in mesostasis regions). Ol is olivine and Px is pyroxene. B) SiO_2 (red)-TiO_2 (green)-Cr_2O_3 (blue) abundances of Dourbes scan 1. The color scale shows SiO_2 abundances between 28.3 wt% and 60.4 wt%, those below 28.3 wt% color are in black and those above 60.4 wt% are om bright red. Cr-rich oxides (blue) occur in olivine (dark red) or at the boundary between olivine and pyroxene (dark red and moderate red) and Ti-rich oxides (turquoise to green) occur in interstitial regions (mesostasis – bright red; secondary –black). Increasing Cr contents are observed in oxides associated with mafic minerals, and lower Cr is observed in oxides in interstitial and mesostasis regions.

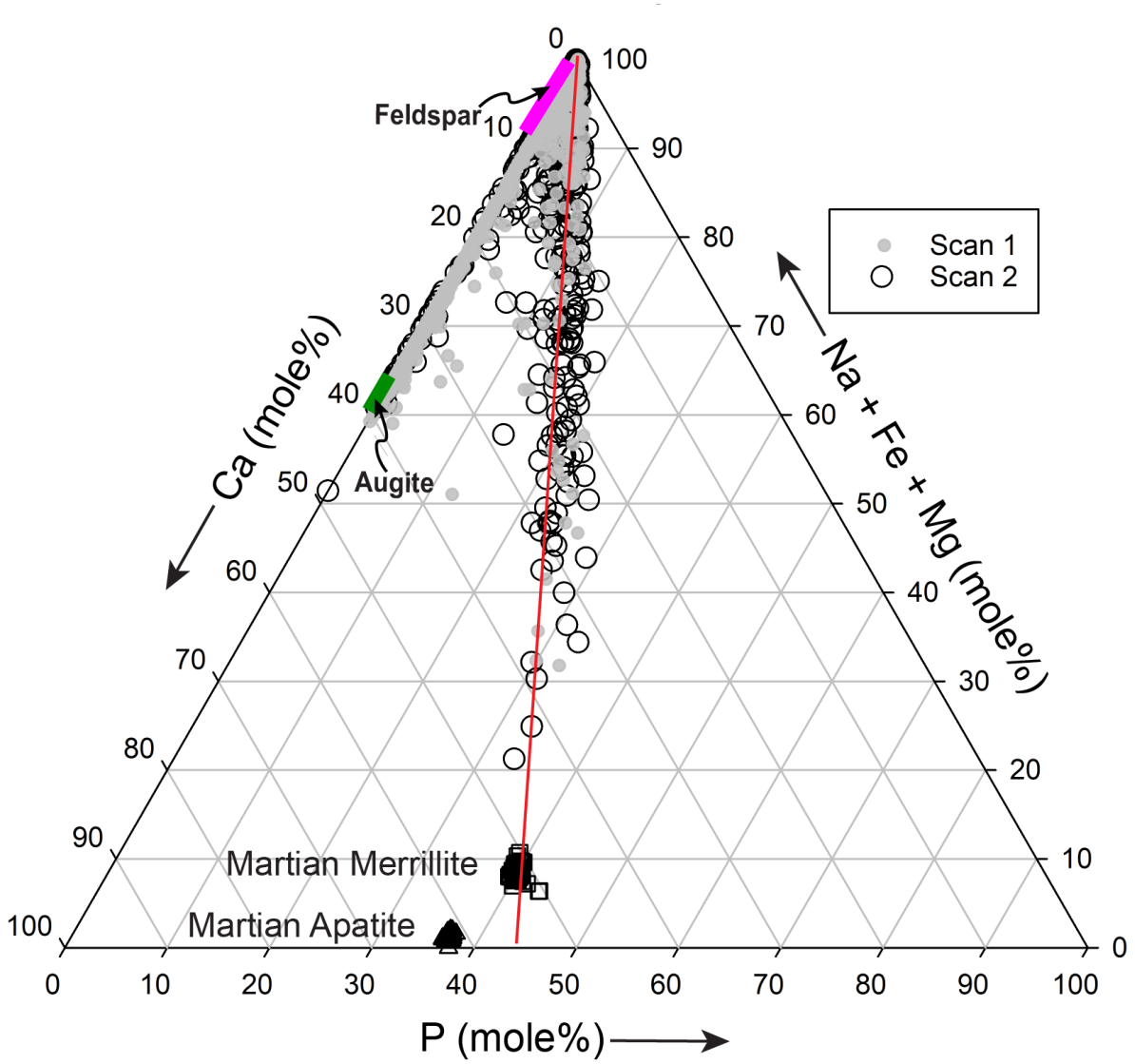

Figure S7. Ternary diagram of selected elements to constrain the phosphate speciecs in Dourbes. Mole values of both scans are plotted. The data points form a sequence (red line) indicating mixing between olivine and augite with a phosphate, likely merrillite. Martian apatite data (open triangles) are from (*27*) and merrillite data (open squares) are from shergotties and Martian breccia NWA 7034/7533 (*45, 91*).

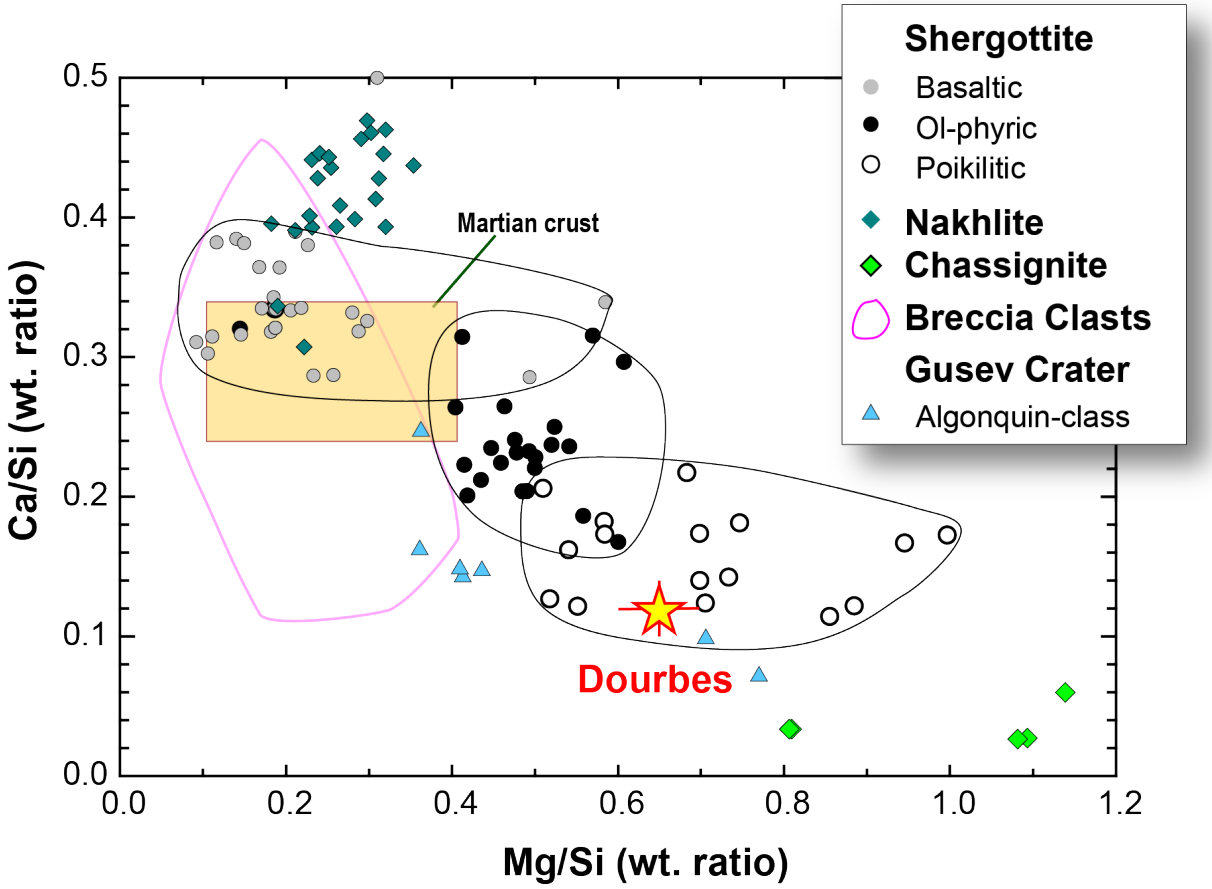

Figure S8. Ca/Si and Mg/Si weight (wt.) ratios for bulk Dourbes, Martian meteorites and the Algonquin rocks at Gusev Crater. There is higher abundance of high-Ca pyroxene and feldspar in the samples with high Ca/Si side, and more olivine in samples with low Ca/Si. Dourbes is most consistent with poikilitic shergottites and olivine-rich Algonquin rocks. Data sources are listed in Table S7.

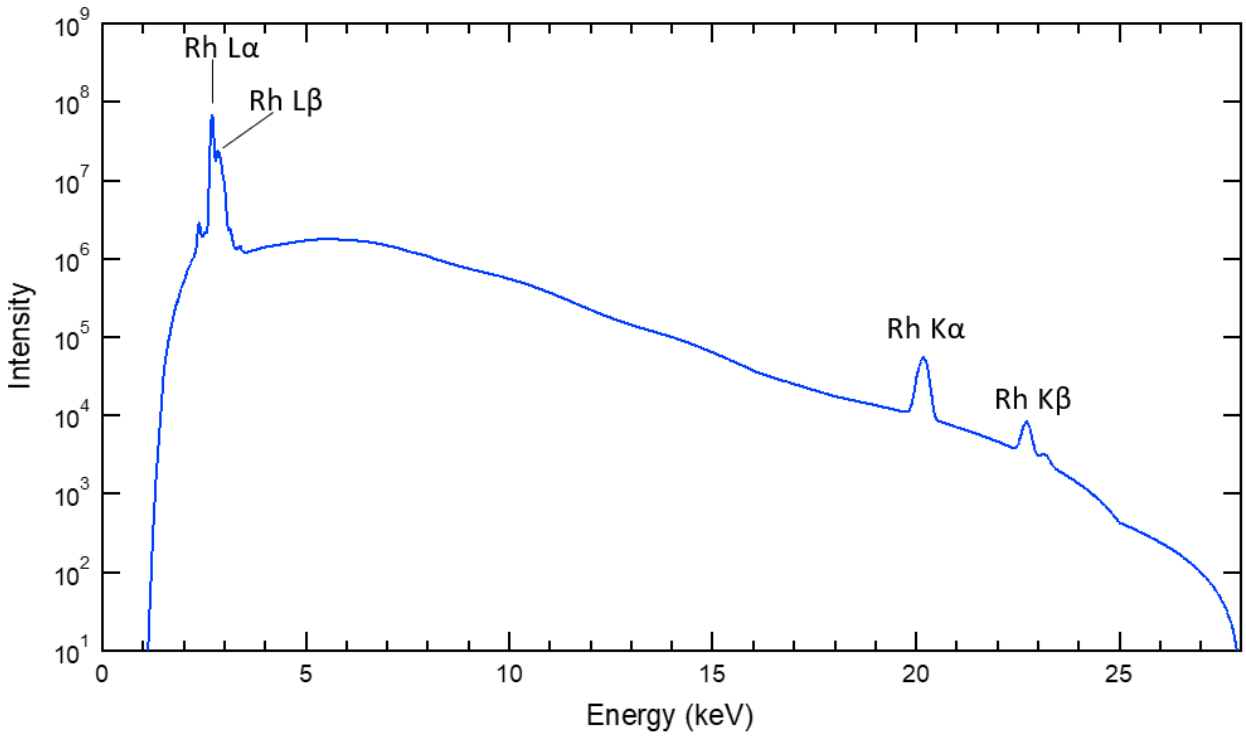

Figure S9. Calculated instrument x-ray spectrum used for PIXL elemental quantification. This includes contributions from the x-ray tube and optics. The primary spectrum has not been directly measured but is inferred from measurements of a Teflon specimen of the same material as the flight Teflon target.

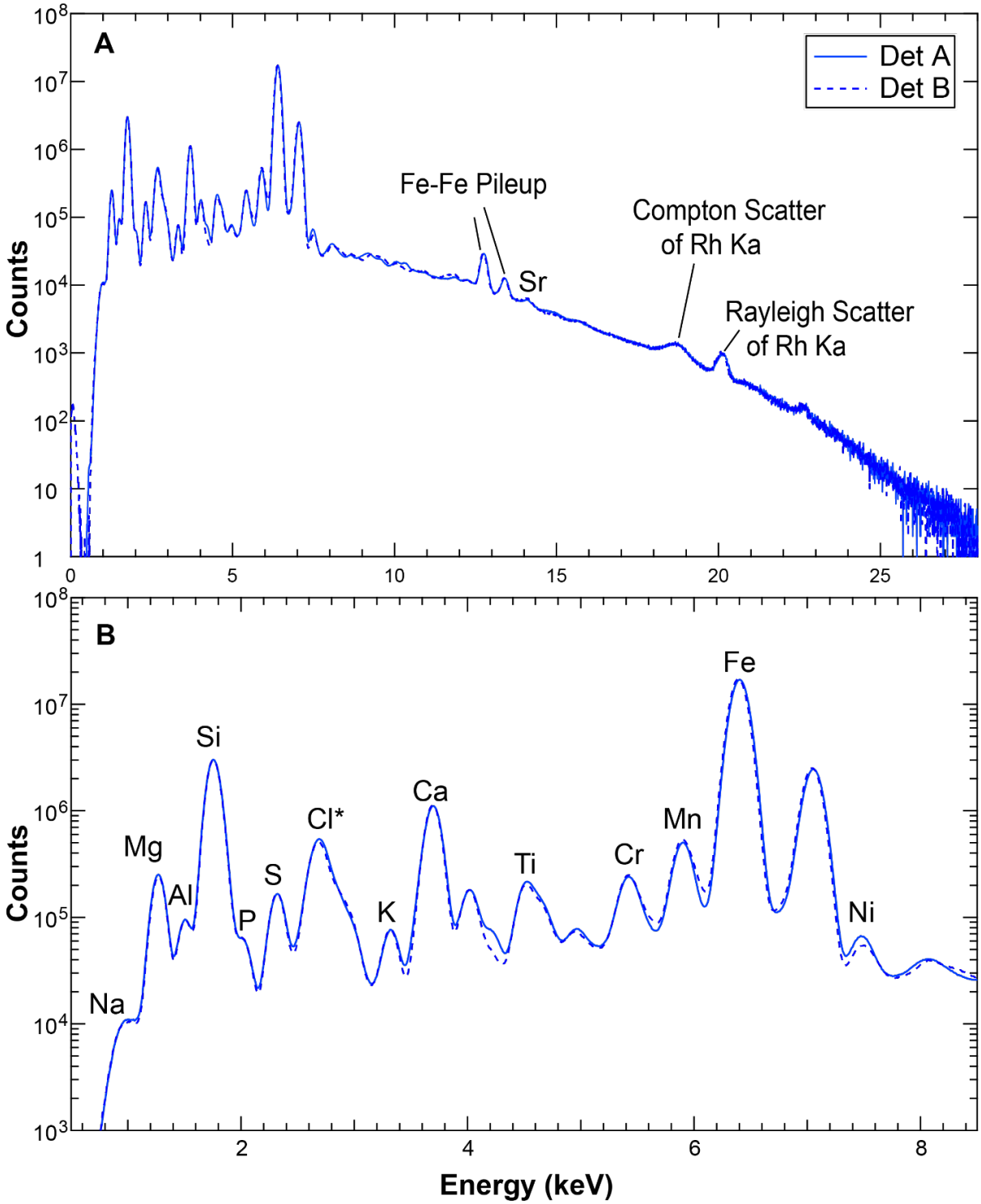

Figure S10. Bulk sum spectra from Detectors A and B (solid and dashed blue lines) for both scans of Dourbes. A)The full spectra. B) A portion of the spectra. The peak labeled by Cl* includes Cl *K*α and Rayleigh scatter of Rh *L*α. Elemental *K*α positions are labelled. The difference between Detector A and B is caused by diffractions peaks, topography, and slightly different responses of Detectors A and B.

Table S1. Mineral modal percentages (vol%) estimated from XRF data and MCC multispectral images.

	XRF data*			MCC G/NIR*				
	Scan 1	**Scan 2**	**Total†**		**Dourbes**		**Garde**	
				Estimate	1	2	1	2
Olivine (Ol)+ Alteration‡	69.2	60.4	65.6	**Olivine+ Alteration ‡**	66	64	65	57
Augite (Aug)	18.0	4.9	12.6	**Augite**	13	15	8	8
Mesostasis	7.4	13.3	9.8					
Secondary	5.4	21.4	12.0	**Secondary & Mesostasis**	31	26	26	34
Original porosity §	**30.8**	**39.6**	**34.4**		34	36	35	43
Ol/(Ol+Aug)	79	93	84		83	81	89	87

***** Uncertainty in XRF data lies in olivine and secondary materials with ± 3 vol%. For MCC G/NIR data, two estimates were obtained by choosing different color ranges. The difference between two estimates can be regarded as uncertainty.

† Total is calculated by combining scan 1 and 2.

‡Alteration regions in olivine are included as olivine.

§ Original porosity is defined as the space between the original olivine grains in the cumulated olivine framework.

Table S2. Elemental abundances for olivine (Ol) in Dourbes. We report the average of quantified points in four olivine grains (Ol 1 to Ol 4). Pristine olivine compositions are calculated by removing salt contamination assuming molar Ca/S and Na/Cl of 1, and then removing excess Na and Al.

	Olivine								**Pristine Olivine**							
	Ol 1		**Ol 2**		**Ol 3**		**Ol 4**		**Ol 1**		**Ol 2**		**Ol 3**		**Ol 4**	
wt%	**n = 33**	**1σ**	**n = 28**	**1σ**	**n = 32**	**1σ**	**n = 16**	**1σ**	**n = 33**	**1σ**	**n = 28**	**1σ**	**n = 32**	**1σ**	**n = 16**	**1σ**
Na_2O	0.54	0.53	0.41	0.39	0.74	0.51	1.11	1.17	0.00	0.00	0.00	0.00	0.00	0.00	0.00	0.00
MgO	25.03	0.79	25.03	0.89	24.52	0.92	25.62	0.88	25.03	0.79	25.03	0.89	24.52	0.92	25.62	0.88
Al_2O_3	0.18	0.17	0.15	0.12	0.23	0.16	0.15	0.14	0.00	0.00	0.00	0.00	0.00	0.00	0.00	0.00
SiO_2	35.52	0.74	35.62	0.54	35.73	0.73	35.20	0.74	35.52	0.74	35.62	0.54	35.73	0.73	35.20	0.74
P_2O_5	0.06	0.07	0.05	0.05	0.05	0.04	0.13	0.04	0.06	0.07	0.05	0.05	0.05	0.04	0.13	0.04
SO_3	0.02	0.02	0.10	0.13	0.02	0.05	0.31	0.08	0.00	0.00	0.00	0.00	0.00	0.00	0.00	0.00
Cl	0.16	0.10	0.38	0.13	0.20	0.13	0.05	0.03	0.00	0.00	0.00	0.00	0.00	0.00	0.00	0.00
K_2O	0.00	0.00	0.00	0.00	0.00	0.00	0.00	0.00	0.00	0.00	0.00	0.00	0.00	0.00	0.00	0.00
CaO	0.23	0.05	0.22	0.08	0.31	0.06	0.37	0.05	0.22	0.04	0.15	0.08	0.29	0.06	0.15	0.06
TiO_2	0.00	0.00	0.00	0.00	0.19	0.13	0.00	0.00	0.00	0.00	0.00	0.00	0.19	0.13	0.00	0.00
Cr_2O_3	0.00	0.00	0.00	0.02	0.00	0.01	0.14	0.07	0.00	0.00	0.00	0.02	0.00	0.01	0.14	0.07
MnO	0.62	0.02	0.56	0.02	0.66	0.05	0.55	0.02	0.62	0.02	0.56	0.02	0.66	0.05	0.55	0.02
FeO_T *	36.60	0.42	36.70	0.52	36.34	0.64	37.35	0.73	36.60	0.42	36.70	0.52	36.34	0.64	37.35	0.73
Total	**99.0**		**99.2**		**99.0**		**101.0**		**98.0**		**98.1**		**97.8**		**99.1**	
Cations	Atoms per 4 oxygen															
Na	0.029	0.029	0.022	0.021	0.041	0.028	0.061	0.064	0.000	0.000	0.000	0.000	0.000	0.000	0.000	0.000
Mg	1.060	0.031	1.059	0.026	1.038	0.035	1.067	0.029	1.067	0.028	1.066	0.026	1.047	0.033	1.084	0.024
Al	0.006	0.005	0.005	0.004	0.008	0.005	0.005	0.005	0.000	0.000	0.000	0.000	0.000	0.000	0.000	0.000
Si	1.010	0.011	1.011	0.012	1.015	0.018	0.983	0.009	1.016	0.013	1.018	0.012	1.023	0.020	0.999	0.009
P	0.001	0.002	0.001	0.001	0.001	0.001	0.003	0.001	0.001	0.002	0.001	0.001	0.001	0.001	0.003	0.001
S	0.000	0.001	0.002	0.003	0.000	0.001	0.007	0.002	0.000	0.000	0.000	0.000	0.000	0.000	0.000	0.000
Cl	0.000	0.000	0.000	0.000	0.000	0.000	0.000	0.000	0.000	0.000	0.000	0.000	0.000	0.000	0.000	0.000
K	0.000	0.000	0.000	0.000	0.000	0.000	0.000	0.000	0.000	0.000	0.000	0.000	0.000	0.000	0.000	0.000
Ca	0.007	0.001	0.007	0.002	0.009	0.002	0.011	0.001	0.007	0.001	0.005	0.003	0.009	0.002	0.005	0.002
Ti	0.000	0.000	0.000	0.000	0.004	0.003	0.000	0.000	0.000	0.000	0.000	0.000	0.004	0.003	0.000	0.000
Cr	0.000	0.000	0.000	0.000	0.000	0.000	0.003	0.002	0.000	0.000	0.000	0.000	0.000	0.000	0.003	0.002
Mn	0.015	0.000	0.014	0.001	0.016	0.001	0.013	0.001	0.015	0.000	0.014	0.001	0.016	0.001	0.013	0.001
Fe	0.870	0.013	0.871	0.012	0.863	0.017	0.873	0.009	0.876	0.012	0.877	0.010	0.870	0.016	0.887	0.009
Total	**2.999**		**2.992**		**2.995**		**3.025**		**2.982**		**2.980**		**2.971**		**2.994**	
Fo	54.9	0.8	54.8	0.8	54.6	0.9	55.0	0.7	54.9	0.8	54.8	0.8	54.6	0.9	55.0	0.7
Fe/Mn †	59	2	64	3	55	4	67	3								

* FeO_T: all Fe is assumed to be Fe^{2+}.

† Fe/Mn is the molar ratio. Because the salt correction did not include any Fe, the ratio may include minor contamination if Fe-oxide weathering product is present.

Table S3. Elemental abundances for pyroxene (Px) in Dourbes. We report the average of quantified points in two regions in one pyroxene grain (Px 1a and Px 1b), and one region in a second pyroxene grain (Px 2). Pristine pyroxene average compositions are calculated by removing salt contamination as above. n is total points, 1σ is the one standard deviation of the average or propagated errors for Wo, En, Fs, and molar Fe/Mn values.

	Pyroxene						Pristine Pyroxene					
	Px 1a [3]		Px 1b		Px 2		Px 1a		Px 1b		Px 2	
wt%	**n = 28**	**1σ**	**n = 58**	**1σ**	**n = 5**	**1σ**	**n = 28**	**1σ**	**n = 58**	**1σ**	**n = 5**	**1σ**
Na_2O*	0.73	0.58	0.77	0.54	0.99	0.83	0.58	0.53	0.65	0.51	0.93	0.81
MgO	15.33	1.01	14.36	0.71	14.51	0.32	15.33	1.01	14.36	0.71	14.51	0.32
Al_2O_3	0.89	0.22	0.96	0.25	0.90	0.12	0.89	0.22	0.96	0.25	0.90	0.12
SiO_2	51.12	3.07	50.13	2.46	51.05	0.79	51.12	3.07	50.13	2.46	51.05	0.79
P_2O_5	0.06	0.09	0.06	0.10	0.04	0.03	0.06	0.09	0.06	0.10	0.04	0.03
SO_3	0.09	0.09	0.05	0.08	0.13	0.18	0.00	0.00	0.00	0.00	0.00	0.00
Cl	0.27	0.17	0.16	0.13	0.07	0.02	0.00	0.00	0.00	0.00	0.00	0.00
K_2O	0.00	0.00	0.00	0.00	0.00	0.00	0.00	0.00	0.00	0.00	0.00	0.00
CaO	16.82	1.56	17.24	0.96	17.83	0.39	16.76	1.57	17.21	0.99	17.74	0.43
TiO_2	0.26	0.06	0.29	0.25	0.33	0.06	0.26	0.06	0.29	0.25	0.33	0.06
Cr_2O_3	0.27	0.06	0.36	0.67	0.28	0.03	0.27	0.06	0.36	0.67	0.28	0.03
MnO	0.33	0.09	0.32	0.10	0.28	0.03	0.33	0.09	0.32	0.10	0.28	0.03
FeO_T †	12.92	1.65	12.27	1.03	12.11	0.31	12.92	1.65	12.27	1.03	12.11	0.31
Total	**99.1**		**97.0**		**98.5**		**98.5**		**96.6**		**98.2**	
Cations	Atoms per 6 oxygen											
Na	0.054	0.043	0.058	0.040	0.073	0.061	0.043	0.039	0.049	0.038	0.069	0.061
Mg	0.872	0.071	0.833	0.036	0.827	0.017	0.874	0.071	0.835	0.037	0.829	0.019
Al	0.040	0.010	0.044	0.012	0.040	0.005	0.040	0.011	0.044	0.013	0.041	0.005
Si	1.946	0.053	1.950	0.043	1.952	0.023	1.951	0.053	1.953	0.043	1.957	0.018
P	0.002	0.003	0.002	0.003	0.001	0.001	0.002	0.003	0.002	0.003	0.001	0.001
S	0.003	0.002	0.001	0.002	0.004	0.005	0.000	0.000	0.000	0.000	0.000	0.000
Cl	0.000	0.000	0.000	0.000	0.000	0.000	0.000	0.000	0.000	0.000	0.000	0.000
K	0.000	0.000	0.000	0.000	0.000	0.000	0.000	0.000	0.000	0.000	0.000	0.000
Ca	0.686	0.050	0.719	0.031	0.730	0.013	0.685	0.050	0.719	0.031	0.729	0.014
Ti	0.007	0.002	0.008	0.007	0.009	0.002	0.007	0.002	0.008	0.007	0.009	0.002
Cr	0.008	0.002	0.011	0.020	0.008	0.001	0.008	0.002	0.011	0.020	0.008	0.001
Mn	0.011	0.003	0.011	0.004	0.009	0.001	0.011	0.003	0.011	0.004	0.009	0.001
Fe	0.414	0.068	0.400	0.038	0.387	0.009	0.415	0.068	0.401	0.039	0.388	0.010
Total	**4.042**		**4.037**		**4.042**		**4.036**		**4.032**		**4.042**	
Wo	34.9	3.5	36.8	1.7	37.6	0.9	34.8	3.5	36.8	1.7	37.4	1.0
Fs	20.9	2.5	20.5	1.8	19.9	0.4	20.9	2.5	20.5	1.8	20.0	0.4
En	44.2	1.8	42.7	1.3	42.5	0.6	44.2	1.8	42.7	1.3	42.6	0.7

Fe/Mn †	39	13	38	13	42	4	

* FeO_T: all Fe is assumed to be Fe^{2+}.

† Fe/Mn is the molar ratio. Because the salt correction did not include any Fe, the ratio may include minor contamination if Fe-oxide weathering product is present.

Table S4. Elemental abundances of mesostasis regions in Dourbes. We report the average of quantified points in six mesostasis regions (Meso1 to Meso6). Large variations of mesostasis reflect the heterogeneous nature of the constituent minerals, especially when a Fe-Cr-Ti oxide is present.

	Mesostasis (Meso)											
	Meso1		**Meso2**		**Meso3**		**Meso4**		**Meso5**		**Meso6**	
wt%	**n = 18**	**1σ**	**n = 22**	**1σ**	**n = 18**	**1σ**	**n = 21**	**1σ**	**n = 11**	**1σ**	**n = 30**	**1σ**
Na_2O	8.55	1.56	7.22	2.09	6.00	1.35	7.60	1.27	6.63	1.43	7.11	2.39
MgO	2.89	1.75	4.85	2.26	7.35	2.92	3.28	1.84	3.60	1.40	3.18	1.46
Al_2O_3	17.31	2.53	14.21	4.42	12.60	2.28	15.14	2.47	14.84	2.02	14.73	4.97
SiO_2	55.00	8.07	52.92	12.94	52.12	3.87	53.50	5.58	52.32	5.55	46.81	17.60
P_2O_5	4.71	7.43	0.81	2.40	2.47	2.41	6.09	3.35	4.78	4.57	1.42	3.78
SO_3	0.23	0.21	0.09	0.05	0.06	0.03	0.12	0.15	0.22	0.22	0.12	0.09
Cl	0.53	0.23	0.37	0.20	0.57	0.17	0.50	0.25	0.80	0.37	0.38	0.35
K_2O	1.59	0.32	1.74	0.73	2.18	0.90	2.11	0.44	2.09	0.35	1.49	0.80
CaO	5.23	6.15	2.22	2.31	2.72	2.42	6.27	3.20	4.48	3.36	2.25	3.60
TiO_2	0.17	0.11	1.64	4.27	0.26	0.20	0.29	0.16	0.15	0.05	3.89	5.36
Cr_2O_3	0.00	0.00	1.43	4.25	0.00	0.02	0.06	0.20	0.15	0.05	3.26	5.03
MnO	0.06	0.07	0.05	0.07	0.11	0.09	0.04	0.05	0.01	0.02	0.06	0.18
FeO_T*	3.19	2.80	8.74	14.94	9.60	6.36	3.48	2.62	3.96	1.91	13.16	16.76
Total	99.46	4.76	96.29	5.78	96.04	4.41	98.48	4.44	94.03	3.77	97.86	4.99

* FeO_T: all Fe is assumed to be Fe^{2+}.

Table S5. Bulk chemistry of PIXL XRF scans of Dourbes. Bulk chemistry is quantified from sum spectra of all points (n is number of points) from both detectors (A+B) or separately (A or B). Uncertainties (1 sigma, 1σ) are derived from the PIQUANT models. Higher uncertainties were applied when the spectral model contained diffraction peaks (see Methods). Differences between detector A and B are smaller than quoted uncertainty, suggesting the diffraction peak effects are small in the bulk data.

	Dourbes – All locations						**Dourbes - Pristine locations** *					
n	**5670**						**3878**					
Detector	**A+B**	**1σ**	**A**	**1σ**	**B**	err	**A+B**	**1σ**	**A**	**1σ**	**B**	**1σ**
Na_2O	1.93	0.70	2.00	0.66	1.83	0.63	1.60	0.62	1.66	0.67	1.54	0.64
MgO	19.24	0.97	19.70	0.99	18.76	0.95	20.27	1.00	20.74	1.05	19.77	1.00
Al_2O_3	2.42	0.55	2.45	0.55	2.39	0.55	2.25	0.54	2.28	0.54	2.22	0.54
SiO_2	39.42	1.98	39.83	2.00	39.02	1.95	40.39	2.02	40.75	2.04	40.02	2.01
P_2O_5	0.48	0.23	0.48	0.23	0.48	0.22	0.42	0.25	0.43	0.24	0.42	0.25
SO_3	0.78	0.27	0.79	0.27	0.78	0.27	0.18	0.18	0.20	0.21	0.16	0.18
Cl	0.66	0.23	0.68	0.24	0.65	0.23	0.32	0.23	0.33	0.23	0.31	0.23
TiO_2	0.37	0.25	0.38	0.18	0.35	0.19	0.39	0.25	0.41	0.16	0.37	0.17
CaO	2.94	0.56	2.96	0.56	2.91	0.56	3.27	0.55	3.32	0.55	3.22	0.56
K_2O	0.18	0.19	0.18	0.25	0.17	0.25	0.15	0.17	0.15	0.24	0.15	0.23
Cr_2O_3	0.26	0.23	0.26	0.23	0.27	0.24	0.30	0.24	0.29	0.24	0.31	0.25
MnO	0.69	0.29	0.65	0.26	0.73	0.31	0.70	0.30	0.65	0.26	0.75	0.30
FeO_T	30.05	1.50	29.81	1.49	30.28	1.51	30.58	1.53	30.30	1.51	30.88	1.54
Total	99.4		100.2		98.6		100.8		101.5		100.1	
Mg#	54		54		53		54		55		54	

* Pristine regions were defined as points that are crystalline (presence of diffraction peaks) and contain SO_3 and Cl concentrations < 1 wt%.

Table S6. Equilibrium temperature between olivine (ol) and augite (aug). Temperature was calculated using the olivine and augite Mg-Fe exchange geothermometer (*44*). Average values of olivine and augite were obtained from those reported in Tables S2-S3. 1σ is the one standard deviations of the average values. The upper and the lower limit of the equilibrium temperature is calculated using the propagated error based on the PIQUANT model uncertainties for Fe and Mg in each phase.

	Average	1σ	**T (°C)**
Molar $(Fe/Mg)_{Ol}$	0.82	0.01	
Molar $(Fe/Mg)_{Aug}$	0.47	0.01	
Molar $(Fe/Mg)_{Ol/Aug}$	1.74*	0.19*	**1085**
Uncertainty of T induced by that of the $(Fe/Mg)_{Ol/Aug}$			
$(Fe/Mg)_{Ol/Aug}$ -upper	1.55		**1112**
$(Fe/Mg)_{Ol/Aug}$ -lower	1.93		**1060**

*$(Fe/Mg)_{Ol/Aug}$ = $(Fe/Mg)_{Ol}/(Fe/Mg)_{Aug}$. And the 1σ uncertainty of this ratio between olivine and augite is estimated using error propagation and 1σ values of Fe/Mg value of olivine and augite, respectively.

Table S7. Image and data sources used in the figures.

Figure 3	**References**
Martian meteorites	*21, 28, 46, 51, 93*
Figure 4	
Martian meteorites	*21, 28, 46, 51, 93*
Gusev	*32, 96, 97*
Gale	*33, 94, 95*
Meridiani	*53*
Figure S7	
apatite	*27*
merrillite	*45, 91*
Figure S8	
Martian meteorites	(see above)
Gale	(see above)
Movie S1	**File name**
WATSON	
	SIF_0253_0689405660_882FDR_N0080000SRLC02501_0000LM
	SIF_0253_0689405813_019FDR_N0080000SRLC01031_0000LUJ01
	SIF_0257_0689757397_902FDR_N0080000SRLC00672_0000LMJ01
	SC3_0257_0689783886_964ECM_N0080000SRLC11360_0000LMJ01,
ACI	SC3_0269_0690849399_257FDR_N0080000SRLC11421_0000LMJ02l
Figure 1	
1A	Map based on Mars Orbiter Laser Altimeter on Mars Global Survey (*98*)
1B	Mars Reconnaissance Oriber Context Camera mosaic of circum-Isidis Planitia Mars Global Survey (*99*)
1D	Mastcam-Z (*100, 104*) right eye mosaic from Sol 255 include the following images collected with a 34 mm focal length R0 (RGB Bayer). The mosaic is portrayed in natural RGB color: ZRF_0255_0689576320_773RAD_N0080000ZCAM08278_0340LMJ01 ZRF_0255_0689576280_738RAD_N0080000ZCAM08278_0340LMJ01 ZRF_0255_0689576242_738RAD_N0080000ZCAM08278_0340LMJ01 ZRF_0255_0689576202_738RAD_N0080000ZCAM08278_0340LMJ01
1E	Mastcam-Z *(100, 104)* right eye image from Sol 259 with a 110 mm focal length and R0 filter. ZRF_0259_0689934499_269RAD_N0080000ZCAM08280_1100LMJ01
1F	ACI of SHERLOC *(101, 103)*: SC3_0257_0689783886_964ECM_N0080000SRLC11360_0000LMJ01

Caption for Movie S1.

Animation overlying the fine-scale structures in the context images of Dourbes with the mineralogical maps from PIXL. The context images are: color mosaic from WATSON and ACI of SHERLOC (101), PIXL MCC G/NIR ratio image (a different color version of Figs. S1B); a false color map including PIXL quantification of FeO_T (red), MgO (green), and Al_2O_3 (blue) (Figs. 2C and S3); and the mineralogical outlines traced from XRF compositional data.